

Penetrating the Deep Cover of Compton Thick Active Galactic Nuclei

N. A. Levenson¹, T. M. Heckman², J. H. Krolik², K. A. Weaver^{2,3}, & P. T. Życki⁴

ABSTRACT

We analyze observations obtained with the *Chandra X-ray Observatory* of bright Compton thick active galactic nuclei (AGNs), those with column densities in excess of $1.5 \times 10^{24} \text{ cm}^{-2}$ along the lines of sight. We therefore view the powerful central engines only indirectly, even at X-ray energies. Using high spatial resolution and considering only galaxies that do not contain circumnuclear starbursts, we reveal the variety of emission AGNs alone may produce. Approximately 1% of the continuum's intrinsic flux is detected in reflection in each case. The only hard X-ray feature is the prominent Fe K α fluorescence line, with equivalent width greater than 1 keV in all sources. The Fe line luminosity provides the best X-ray indicator of the unseen intrinsic AGN luminosity. In detail, the morphologies of the extended soft X-ray emission and optical line emission are similar, and line emission dominates the soft X-ray spectra. Thus, we attribute the soft X-ray emission to material that the central engines photoionize. Because the resulting spectra are complex and do not reveal the AGNs directly, crude analysis techniques such as hardness ratios would mis-classify these galaxies as hosts of intrinsically weak, unabsorbed AGNs and would fail to identify the luminous, absorbed nuclei that are present. We demonstrate that a three-band X-ray diagnostic can correctly classify Compton thick AGNs, even when significant soft X-ray line emission is present. The active nuclei produce most of the galaxies' total observed emission over a broad spectral range, and much of their light emerges at far-infrared wavelengths. Stellar contamination of the infrared emission can be severe, however, making long-wavelength data alone unreliable indicators of the buried AGN luminosity.

¹Department of Physics and Astronomy, University of Kentucky, Lexington, KY 40506; levenson@pa.uky.edu

²Department of Physics and Astronomy, Bloomberg Center, Johns Hopkins University, Baltimore, MD 21218

³Code 662, NASA/GSFC, Greenbelt, MD 20771

⁴Nicolaus Copernicus Astronomical Center, Bartycka 18, 00-716 Warsaw, Poland

Subject headings: Galaxies: active — galaxies: Seyfert — X-rays: galaxies

1. Introduction

Accretion onto supermassive black holes powers active galactic nuclei (AGNs), but intervening material prevents direct views of most sources. The Compton thick AGNs, which have column density $N_H > 1.5 \times 10^{24} \text{ cm}^{-2}$ along the line of sight to the nucleus, can be particularly elusive, but these AGNs are astrophysically important. First, they are common, representing up to half of all Seyfert 2 galaxies (Risaliti, Maiolino, & Salvati 1999). Second, in synthesis models (e.g., Setti & Woltjer 1989; Comastri et al. 1995), they are essential to replicate the observed spectrum of the cosmic X-ray background, which peaks around 30 keV (Marshall et al. 1980).

The intrinsic X-ray continuum of an AGN up to about 100 keV may be described by a power law, typically of photon index $\Gamma = 1.9$, or spectral index $\alpha = 0.9$ (Nandra & Pounds 1994). Intervening material preferentially absorbs soft X-ray photons, and the direct emission of the central engine is not detectable below 10 keV in Compton thick cases. In the obscuring medium, however, the intrinsic emission is strongly reprocessed. It emerges with an effective flat photon index and diminished intensity, less than about 1% of the intrinsic source luminosity. Thus, Compton thick AGNs easily fall below detection limits of current X-ray surveys, although the intrinsic power of their central engines is not exceptionally feeble. These uncounted sources are responsible in part for the diminishing fraction of the X-ray background that is resolved toward higher energies (Worsley et al. 2005).

In a Compton thick AGN, the large equivalent width (EW) of the Fe K α fluorescence line is the most direct signature of its nuclear activity below 10 keV (Ghisellini, Haardt, & Matt 1994; Krolik, Madau, & Życki 1994). The energy of this line is 6.4 keV when the fluorescing medium is not fully ionized (less than Fe XVIII), or around 6.7 and 7.0 keV in Fe XXV and Fe XXVI, respectively. This line can also be an effective diagnostic of the geometry of the obscuring medium and the AGN’s luminosity (Levenson et al. 2002).

With the powerful continuum suppressed at lower energies, obscured AGNs reveal other soft X-ray spectral components. The active nucleus may produce line emission through photoionization and photoexcitation (Sako et al. 2000; Kinkhabwala et al. 2002; Ogle et al. 2003). The AGN may also drive an outflow that generates shocks in the surrounding medium, producing thermal emission. Alternatively, separate additional emission sources may be present. Specifically, compact circumnuclear starbursts are common in active galaxies (Cid Fernandes, Storchi-Bergmann, & Schmitt 1998; González Delgado, Heckman, & Leitherer 2001).

and they characteristically exhibit soft thermal X-ray spectra (Levenson et al. 2001), similar to starburst galaxies. Here we analyze seven high spatial resolution X-ray observations of optically-bright, Compton thick Seyfert 2 galaxies to identify X-ray and multiwavelength signatures of their obscuration and to measure the power of their hidden central engines.

We define the sample in §2. We present the data and describe new results from the images in §3. With the spectroscopy results (§4), we use the Fe K lines to determine properties of the buried AGNs, identify the soft X-ray emission as a consequence of photoionization, relate the soft X-rays to the continuum emission, and develop coarse X-ray discriminants of Compton thick AGN (§5). We discuss the reflection geometry of the continuum in §6. We use infrared (IR) and optical data to compare the observable and intrinsic characteristics of these galaxies across the electromagnetic spectrum (§7), and we summarize our conclusions in §8.

2. Sample Members

All sample galaxies are classified as normal Seyfert 2s on the basis of optical emission line ratios. We require that the sample members be previously identified as Compton thick and have bright AGNs, based on the core [O III] λ 5007 line flux. The latter criterion allows us to measure the nuclear properties well. In order to reveal the variety of X-ray emission for which an AGN alone may be responsible, we exclude galaxies that are known to contain nuclear starbursts. Furthermore, to separate the immediate nuclear and circumnuclear environments, we require high spatial resolution, which only *Chandra* can provide. The exclusion of galaxies that contain starbursts and the spatial resolution requirement render this sample of Compton thick AGNs smaller than that of other recent work (such as Guainazzi et al. 2005a), but these restrictions allow us to isolate the active nuclei and therefore recover their intrinsic properties accurately. Data are then available for seven galaxies, down to core [O III] flux limit of 7×10^{-13} erg s $^{-1}$. We rely on Whittle’s (1992) [O III] fluxes, where available. We use the [O III] fluxes of ESO 428-G14, NGC 3393, and NGC 5347 from Bergvall, Johansson, & Olofsson (1986), Diaz, Prieto, & Wamsteker (1988), and González Delgado & Perez (1996), respectively. The sample is listed in Table 1.

Koyama et al. (1989) measured a large EW Fe line in a *Ginga* spectrum of NGC 1068 and argued that the direct AGN continuum must therefore be completely blocked. Maiolino et al. (1998) identified ESO 428-G14, NGC 1386, and NGC 3393 as Compton thick in *BeppoSAX* observations. In the first, they noted the flat ($\Gamma = 0.57$) spectrum, low ratio of observed 2–10 keV to [O III] λ 5007 flux, and non-detection above 15 keV as indirect evidence for $N_H > 10^{25}$ cm $^{-2}$. In the second, they fit the 1–10 keV spectrum with a reflection

model and a prominent Fe $K\alpha$ line. They fit the 1–80 keV spectrum of NGC 3393 to find $N_H > 10^{25} \text{ cm}^{-2}$. Risaliti et al. (1999) identified NGC 5347 as Compton thick on the basis of the large Fe $K\alpha$ EW measured in a spectrum from *ASCA* and the low ratio of observed X-ray/[O III] flux. Risaliti et al. (2000) suggested that NGC 7212 is Compton thick from analysis of a low signal-to-noise *ASCA* spectrum, finding an apparently flat continuum and a prominent Fe line. Guainazzi, Matt, & Perola (2005b) confirm this identification in a higher quality spectrum obtained with *XMM-Newton*. Awaki et al. (1991) first measured the large column density and prominent Fe K line of Mrk 3 in a spectrum they obtained using *Ginga*.

Population synthesis analysis of optical spectra shows intermediate-aged and older stellar populations (ages > 100 Gyr) in the nuclei of nearly all sample members (Cid Fernandes et al. 2001, 2004, and references therein). The exception, NGC 5347, exhibits no significant emission from polycyclic aromatic hydrocarbons at $3.3\mu\text{m}$ (Imanishi 2003) and far-infrared (FIR) colors that are characteristic of AGNs (de Grijp, Lub, & Miley 1987). Thus, we do not expect any significant stellar contributions to the X-ray spectra of these galaxies.

3. Observations and Image Analysis

We observed the galaxies using the *Chandra* Advanced CCD Imaging Spectrometer (ACIS) back-illuminated S3 detector. We reprocessed all data from original Level 1 event files using Chandra Interactive Analysis of Observations (CIAO) software, version 3.2. (See the *Chandra* Science Center⁵ for details about *Chandra* data and standard processing procedures.) We applied current calibrations (Calibration Database version 3.0), including corrections for charge-transfer inefficiency and time-dependent gain variations, to produce the Level 2 event files. In each case, we included only good events that do not lie on node boundaries, where discrimination of cosmic rays is difficult. We examined the lightcurves of background regions and excluded times of significant background flares.

In the NGC 1068 observation, we use only the data with 0.1 s “frame times.” With the CCDs read out after very short exposures, we minimize the problem of “pileup,” in which coincident photons that arrive within a single CCD readout are not measured accurately. We otherwise applied the same data reduction procedures described above. This particular observation and observing mode required a correction to the on-source exposure⁶, for a net exposure of 1.53 ks. Mrk 3 was observed with the High-Energy Transmission Grating in place.

⁵<http://cxc.harvard.edu/>

⁶http://cxc.harvard.edu/ciao/caveats/acis_interleave.html

We therefore do not analyze the extended emission of this galaxy, and we refer to published measurements of the spectrum (Sako et al. 2000) where comparisons are appropriate.

Table 1 lists observation dates and resulting exposure times of the data we analyze directly along with some basic information about all of these galaxies. The Galactic column density toward each source (N_H ; column 4) is based on the Schlegel, Finkbeiner, & Davis (1998) measurements of A_V , with $N_H = 1.9 \times 10^{21} A_V \text{ cm}^{-2} \text{ mag}^{-1}$. We use $H_0 = 70 \text{ km s}^{-1} \text{ Mpc}^{-1}$ and redshift (z ; column 5) to derive distances (column 6) and physical scales (column 7).

The *Chandra* image of ESO 428-G14 (Figure 1) is typical. The images clearly show extended X-ray emission, demonstrating that the unresolvable central engine is not the sole observed X-ray source. The resolved emission extends over scales of hundreds of parsecs, and it is predominantly soft. We compare images at soft (0.3–1 keV), medium (1–4 keV), and hard (4–8 keV) energies with corresponding models of *Chandra*'s point spread function. ESO 428-G14, NGC 1068, NGC 1386, and NGC 3393 are significantly extended in the soft and medium bands, even on small (1'') scales, while their hard bands are unresolved. NGC 7212 is significantly extended only in the medium band. The bright center of NGC 5347 is not resolved in any band, although this galaxy shows distinct emission approximately 3'' to the northeast of the nucleus.

In all cases, the large-scale extended X-ray emission appears similar to images of these galaxies in optical emission lines (Figure 2), as Bianchi, Guainazzi, & Chiaberge (2006) have shown for some of these sample members. For example, the morphology of ESO 428-G14 in X-rays specifically and in detail resembles that of both $H\alpha$ and [O III] (Falcke et al. 1996). From the nucleus (evident at both radio and X-ray energies), very bright emission extends toward the northwest, with fainter emission extending toward the southeast. In Figure 2, we show the *Chandra* intensity contours overlaid on the continuum-subtracted $H\alpha$ image obtained with the *Hubble Space Telescope* (*HST*) Planetary Camera of the Wide Field and Planetary Camera 2 (WFPC2). We aligned and scaled the image through the F814W filter (U2NP0603T) to subtract continuum from the F658N image (U2NP0601T). We then aligned the X-ray-identified nucleus (§4) with the maximum optical continuum emission. The maximum broad-band X-ray emission is located north of the Fe $K\alpha$ emission peak that defines the X-ray center. Thus, the highest-intensity contours are not centered on the optical nucleus. Photoionization by the central engine produces the optical line emission in all these galaxies. While the lower spatial resolution X-ray observations cannot show variations on the very small scales (0'.1) that are evident in the optical data, the similar overall X-ray morphology suggests that photoionization is also the origin of the soft X-ray line emission. The *Chandra* spectra also support this interpretation of the line emission as a consequence

of radiative processes rather than collisional excitation as (§5.2).

We find several sources in addition to the active nucleus near each galaxy’s center. We present these results in Appendix A.

4. Spectroscopy

The ACIS data afford spatially resolved spectroscopy of several interesting regions. We obtained spectra of the nuclei, extended circumnuclear regions, and the whole galaxies. We identified the locations of the AGNs in continuum-subtracted Fe K α images. Line emission dominates the emission in images extracted with energy restricted $6 < E < 7$ keV. We measure the corresponding continuum in the bandpass $4.5 < E < 5.5$ keV, at which the ACIS response is similar. We smoothed each of these images by a Gaussian of FWHM = 1”, then subtracted the continuum (4.5–5.5 keV) image from the corresponding line+continuum (6–7 keV) image without any further scaling. This procedure is adequate to determine the locations of the maximum Fe K α emission, but we do not use these images for quantitative measurements of the line flux. The hard X-ray peaks measured in the continuum-subtracted images are listed in Table 1.

To isolate the AGN emission, we extracted spectra within an aperture of 1”5 radius centered on each of these nuclear locations. Even in nearby galaxies, however, these unresolved “nuclear” apertures cover hundreds of parsecs around the active nuclei. While spectroscopy of large regions of some of these sample members has been presented elsewhere (Young, Wilson, & Shopbell 2001; Bianchi et al. 2006), the small nuclear apertures are critical in order to measure the immediate AGN emission, especially the Fe K α line flux and EW. In all cases, we subtracted the background measured in nearby areas that contain no obvious sources. Over the course of the *Chandra* mission, the soft X-ray sensitivity has diminished, likely the result of build-up of material on the detector. We created ancillary response files that account for this time-varying effect. We performed the model fitting in XSPEC (Arnaud 1996).

Broadly, the nuclear spectra are similar. The hard X-ray emission ($E > 3$ keV) is spectrally flat and relatively weak, with a prominent Fe K α emission line in each case. The bright soft X-ray spectra show line emission. In order to measure the Fe K line accurately and to isolate the AGN continuum, we first fit the spectra from only 4–8 keV. We fit unbinned spectra using the *C* statistic (Cash 1979) to retain significant counts at energies greater than 6.5 keV. We model the Fe line as an unresolved Gaussian, accounting for each galaxy’s redshift in measuring the central energy of the line.

The observed flat hard X-ray spectra and previous evidence for Compton thick obscuration indicate that we cannot directly detect the intrinsic AGN power law continuum in these cases. Instead, we model the observed continuum as purely reflected AGN light in a neutral medium using the PEXRAV model (Magdziarz & Zdziarski 1995) in XSPEC. Within the *Chandra* bandpass, we are not sensitive to some of the model parameters (e.g., intrinsic photon index and high-energy cutoff), and others are degenerate. Thus, we fit only for normalization of the intrinsic power law, fixing the remainder of the model parameters: intrinsic photon index $\Gamma = 1.9$, high-energy cutoff = 300 keV, and abundances are solar (Anders & Grevesse 1989). The model describes reflection off a plane-parallel, semi-infinite slab, and it is a function of viewing angle, measured from the slab normal. We adopt inclination $i = 63^\circ$, the model default. This is an intermediate value considering obscured views only; assuming a toroidal obscuring geometry with half-opening angle θ , the central engine is not viewed directly from $i = \theta$ to 90° . Although the high-energy ($E > 10$ keV) spectral shape varies with viewing angle, the primary effect on the *Chandra* spectra is to alter the normalization. Compared with the extreme values, the adopted inclination angle results in normalizations that may be overestimated by up to 25% (for true pole-on views) or underestimated by up to a factor of three (for equatorial views). We also account for Galactic absorption, although its effect is negligible.

Table 2 contains the results of these hard nuclear fits, including the C statistic and number of degrees of freedom (*dof*). The tabulated values of the power law normalization (column 5) assume full (100%) reflection of the AGN continuum. With decreasing relative reflection, (e.g., with smaller covering fraction of reflecting material), the underlying AGN normalization increases proportionally. Figure 3 shows the hard spectral fits; the prominent Fe lines are evident in all these nuclear spectra.

At the current sensitivity and resolution, there are no significant spectral differences among an intrinsic (heavily absorbed) continuum, this reflection model, and an unabsorbed $\Gamma = 0$ power law. For example, the Fe absorption edge is strongest in the first of these models and absent in the last, but the edge cannot be distinguished in any of these data. The shortcoming of the flat power law is that this model is purely phenomenological; such intrinsic spectra are not observed in Seyfert 1 galaxies or less-obscured Seyfert 2s, where they would be detectable. The advantage of adopting the reflection model is that it does provide a lower limit on the intrinsic AGN power, which we will compare with other multiwavelength observations and calculations (§7).

The soft X-ray spectra do not affect the high-energy results, so for simplicity, we fixed these latter model components while fitting the spectra over the full 0.4–8 keV range. We grouped the full spectra into bins having a minimum of 20 counts each and use the χ^2

statistic. While fixing foreground extinction at the Galactic values, we considered several physically-motivated model components to account for the soft X-rays: the MEKAL thermal model (Mewe, Gronenschild, & van den Oord 1985; Mewe, Lemen, & van den Oord 1986; Liedahl, Osterheld, & Goldstein 1995), additional power laws, and line emission. An AGN-driven outflow may generate thermal emission. The non-thermal continuum may be the intrinsic continuum reflected off the surrounding medium. Photoionization by the AGN continuum may produce recombination and fluorescence lines.

Overall, we find that the line emission dominates the nuclear spectra below 3 keV. While the ACIS detector cannot resolve individual transitions, the spectra show relatively sharp emission peaks, as opposed to the much broader blends of many lines that collisional excitation would exhibit. We model these lines as unresolved Gaussians. In each spectrum, we include additional lines or other components as long as they are significant at the 95% confidence level, based on an F test. Figure 4 of ESO 428-G14 is representative of the full nuclear spectra and the best-fitting models. We emphasize that predominantly thermal models do not quantitatively fit any of the observed spectra as well as these line models do (§5.2).

We consider the spectra of extended regions of the galaxies. (We exclude NGC 1068 from this discussion because its extended X-ray emission has been extensively analyzed previously; Young et al. 2001.) We extracted spectra from the bright, central regions of the galaxies, including their nuclei. These elliptical apertures are $6'' \times 3''$ in NGC 1386 and NGC 3393, and $5'' \times 3''.5$ and $3''.5 \times 2''$ in ESO 428-G14 and NGC 7212, respectively. We also obtained a spectrum of the soft X-ray emission northeast of the nucleus of NGC 5347, within a circular aperture of $1''.5$ radius. The total emission within $1'$ of each nucleus yields a spectrum of each galaxy as a whole.

Tables 3 and 4 list the results of these model fits of the soft nuclear spectra and the larger central regions where our findings are new or significantly different from published values, and Table 5 summarizes the flux measurements. Some of the spectra do require model components in addition to the unresolved lines and hard X-ray features. The central ESO 428-G14 spectrum requires an additional continuum source, which a power law describes well. Because the power law index is not well constrained, however, we fix its slope at 1.9, matching the intrinsic AGN continuum.

Given the limited spectral resolution of the detector, each modeled line in the soft spectrum represents a blend of emission lines and is not attributable to a single transition. However, we identify a particular element as the dominant emitter in several cases where the observed line energy corresponds to a known (measured or theoretical) value. For example, in all spectra we find emission near 0.56 and 0.91 keV, which we identify as O VII and Ne IX,

respectively. Several of the spectra suggest Si XIII near 1.8 keV. We do not characteristically find emission from fully-ionized species, although we measure O VIII in NGC 1386 and it may appear blended in the spectrum of ESO 428-G14. Ne X may also contribute to the lines observed at 1.0 keV in several of the spectra. Most of the lines observed to have energies between 0.7 and 1.2 keV likely contain a strong contribution from the many Fe L shell lines in this energy range.

The best-fitting models of the NGC 3393 nuclear and central spectra each include a thermal component. At this temperature, ($kT \approx 1.6$ keV), the collisional excitation results in a number of emission lines around 1 keV, where Fe L transitions are also strong. We considered adding to the unresolved lines a broad Gaussian emission feature, to account for the many Fe L lines, instead of the thermal component. The model with the thermal component fits the data much better than this alternate purely descriptive model. In the nuclear spectrum, for example, $\chi^2/\nu = 25/21$ for Gaussian width $\sigma = 0.3$ and central energy 0.9 keV. We note that both our hard and soft spectral fits differ from the results of Bianchi et al. (2006). The larger Fe K α EW we find may be a consequence of our smaller aperture, selected to isolate the line emission against the AGN’s continuum. We do not, however, significantly measure as many unresolved soft lines as they report, even in our larger aperture.

The emission northeast of the NGC 5347 nucleus is distinct, but faint. Only the soft X-ray flux is significant. A single-temperature thermal model fits the unbinned spectrum of this region, with $kT = 0.24 \pm 0.05$, although optical line ratios indicate that this emission is photoionized (González Delgado & Perez 1996).

We fit the whole galaxy spectra with models based on the best-fitting nuclear and central models, freeing the both the hard and soft X-ray parameters. These spectra cover very large areas, so they contain the integrated flux of many different emission sources. We do not interpret the physical significance of the models in detail, but use these results for flux comparisons (Table 5).

Most of the total flux is located within the smaller (central and nuclear) regions, rather than extended throughout the host galaxies. The central regions account for more than 70% of each galaxy’s total soft emission. Typically, the nuclear aperture alone contains most of the soft emission. NGC 3393 is exceptional; here less than 40% of the soft flux is contained within the nucleus, and the larger (1700×770 pc) central area accounts for the plurality of this galaxy’s soft emission. In each case, the nucleus alone does provide at least half of the total observed galactic hard X-ray emission (measured within a $1'$ radius aperture). In most cases, however, the *extra*-nuclear fraction of observed hard X-rays is significant, around 40% to 50%. In a less-obscured active galaxy, nearly all of the hard X-rays would be detected in

the immediate vicinity of the unresolvable central engine, because the hard AGN continuum would be observed directly. In this group of Compton thick sources, the spectra show that the hard X-rays emerge indirectly. As a result, line emission at energies greater than 2 keV is significant and may arise on larger physical scales. Only in NGC 5347 is the net (line and continuum) reprocessing confined to a small region (radius < 300 pc).

We estimate that X-ray binaries contribute a small fraction of the observed total hard X-ray flux of the whole galaxies we measured. Colbert et al. (2004) derive scaling relations for the 0.3–8 keV flux of unresolved sources in terms of galaxy luminosity measured at FIR, K , and UV wavelengths. To determine the UV luminosity, we use *IUE* observations of NGC 3393 (Kinney et al. 1993). In the other cases, we very roughly estimate this value from observations at B , assuming $f_{2000\text{\AA}}/f_{4400\text{\AA}} = 0.2$ (Kinney et al. 1996). We find that the 0.3–8 keV flux of X-ray binaries is less than about 10% of the total 2–10 keV flux. Modeling the typical source as a power-law ($\Gamma = 1.8$) spectrum with Galactic absorption, we conclude that the 2–10 keV flux of such point sources is less than 5% of the total 2–10 keV flux of each galaxy.

5. Results

5.1. Fe $K\alpha$ Line Emission: An Indicator of the Intrinsic Nuclear Luminosity

The line emission near 6.4 keV is the most significant X-ray characteristic of the AGNs in these galaxies. All of the line central energies are consistent with Fe $K\alpha$ in a “neutral” medium, i.e., less ionized than Fe XVIII. To remain neutral, the fluorescing medium must not receive the powerful ionizing flux of the central engine directly, and it is likely the torus of the unified AGN scenario (Antonucci 1993), the same region that blocks broad optical emission lines from direct view in these Seyfert 2s.

The line EW is a function of obscuring column density, covering fraction, and viewing angle (Krolik et al. 1994). Qualitatively, larger covering fraction produces larger EW, since more Fe-edge photons are captured and generate $K\alpha$ photons. The continuum is most suppressed along the equatorial plane, so these viewing angles also result in larger EWs. The large equivalent widths confirm the Compton thick identification of these AGNs. At solar abundance, EWs larger than 1 keV require $N_H > 1.5 \times 10^{24} \text{ cm}^{-2}$.

The EWs place some limits on the covering fraction, dependent on the viewing angle, i (Krolik et al. 1994; Levenson et al. 2002). In these models, the intrinsic AGN spectrum has $\Gamma = 1.9$, and the obscuring torus has a square cross-section allowing for unobstructed views over half-opening angle θ . An EW < 1.5 keV does not strongly constrain the covering

fraction, yielding $\theta \lesssim 50^\circ$. With the large EWs of ESO 428-G14 and NGC 1386, we find $\theta < 35$ and 20° for modest viewing angle ($i = 65^\circ$), and $\theta < 45$ and 30° , respectively, viewed almost through the equatorial plane ($i = 85^\circ$).

The results of these numerical simulations also show that the Fe line luminosity and the intrinsic AGN luminosity are related. For each of the observed AGNs, we use these numerical models to find the region in inclination angle, covering fraction, and column density parameter space consistent with the measured EW and its errors. We then compute the mean ratio of Fe $K\alpha$ to intrinsic continuum luminosity within this portion of parameter space. We typically find $L_{Fe}/L_{AGN,2-10} \approx 2 \times 10^{-3}$, where $L_{AGN,2-10}$ is the AGN’s intrinsic 2–10 keV luminosity. Table 6 lists L_{Fe} (column 4) and the resulting values of $L_{AGN,2-10}$ (column 5). We label this intrinsic 2–10 keV luminosity $L_{AGN,Fe}$ to distinguish it from the intrinsic luminosity we determine using other techniques. Typical of Seyfert galaxies, the outcome is $L_{AGN,Fe} \sim 10^{42} \text{ erg s}^{-1}$. In all cases, the observed 2–10 keV luminosity represents only about 1% of the intrinsic luminosity ($L_{obs,2-10}/L_{AGN,Fe} \approx 0.01$.) Note that the observed luminosities $L_{obs,0.5-2}$ and $L_{obs,2-10}$ in Table 6 are *not* corrected for any absorption; they correspond to the directly-detectable flux of the sources.

Having the same underlying energy source, $L_{AGN,2-10}$ and $L_{[OIII]}$, the luminosity of the [O III] λ 5007 line, are correlated. Our Fe K estimates of the intrinsic luminosity are consistent with this empirical relationship (Table 6, column 7). Specifically, we consider the Heckman et al. (2005) result $\log(L_{AGN,2-10}/L_{[OIII]}) = 1.59 \pm 0.48$ for the optically-selected type 1 AGNs. (These unobscured nuclei reveal the intrinsic relationship, without the significant correction for X-ray absorption that even the Compton thin type 2 AGNs require.) Figure 5 illustrates the agreement of the Fe line and [O III] estimates of intrinsic AGN luminosity. In addition to the sample members, which are uncontaminated by nuclear starbursts, we also plot the published results for two Compton thick galaxies that do contain starbursts (Levenson et al. 2004, 2005). The dotted line is plotted at a luminosity ratio of one, not a fit to the data.

We compare the NGC 3393 results with the *BeppoSAX* detection in the 15–220 keV band with the Phoswich Detector System (PDS) as a direct measurement of the intrinsic AGN. We use only the high-energy data to measure the intrinsic AGN continuum level, neglecting the lower-energy measurements, which include multiple emission sources. We use the pipeline processed data, fitting the standard grouped spectrum from 15 to 220 keV. Both power law and cutoff power law models fit the data, with $\Gamma \approx 2$. Extending these models to the *Chandra* bandpass, we find $F_{AGN,2-10} = 6 \pm 2 \times 10^{-11} \text{ erg cm}^{-2} \text{ s}^{-1}$, or $L_{AGN,2-10} = 2 \pm 1 \times 10^{43} \text{ erg s}^{-1}$, in reasonable agreement with the Fe line calculation. Maiolino et al. (1998) and Guainazzi et al. (2005a) also use the *BeppoSAX* data obtained with multiple instruments over a broader

energy range and obtain similar results. Most importantly, their analyses explicitly show the Compton thick obscuration and characteristic reflected spectrum that we detect below 8 keV.

5.2. Origin of the Soft X-rays: Extra-Nuclear Photoionized Gas

The morphology (§3 and Bianchi et al. 2006) and spectra (§4) of the soft X-ray emission provide evidence that we observe photoionized material. The extended features of the X-ray images match those of optical images. In the spectra, we find that a limited number of strong lines produce the observed features, in contrast to broad line complexes that would be observed from thermal plasma at the current spectral resolution, as we demonstrate quantitatively here. Radiation (from the AGN) rather than collisions thus determines the ionization state of the emitting material. We therefore describe this gas as photoionized, although other radiative processes, including photoexcitation and resonant scattering, likely produce some of the observed lines.

Figure 6 illustrates the general deficiency of the thermal models in describing these soft spectra, using ESO 428-G14 as an example. The best-fitting thermal soft X-ray model ($kT = 0.70$ keV) fits poorly ($\chi^2/\nu = 131/42$). It results in a broad emission peak around 0.9 keV, and it cannot reproduce the individual narrower peaks around 0.8, 0.9, and 1.1 keV that are evident at the present resolution. Two thermal components can fit the spectrum well; with $kT = 0.63$ and 2.1 keV, $\chi^2/\nu = 38/40$. In this case, however, the difficulty would be to account for the hot component in a physically reasonable way. Shock velocities of nearly 1500 km s^{-1} would be required, yet there is no evidence for the corresponding broad line widths in either these spectra or high-resolution spectra of other active galaxies, where they could certainly be detected. Purely thermal models produce similar results in the nuclear spectra of the other sample members. In summary, physically reasonable thermal models do not quantitatively fit the spectra well.

Thermal emission can be identified and measured in CCD X-ray spectra when it is present. Starburst galaxies, for example, contain large volumes of hot gas, often in a galactic-scale wind (Heckman et al. 1990). Detailed analysis of *Chandra* ACIS observations of the starburst galaxy NGC 253 clearly shows thermal emission (Strickland et al. 2002). In this case, a two-temperature model (with $kT = 0.2$ and 0.7 keV) fits spectra of the diffuse emission well, although it requires low abundances.

NGC 1068 serves as a useful example of photoionized material, in which radiative processes produce the soft X-ray line emission. This brighter galaxy has been successfully

observed at high spectral resolution. Measurements of the strength of individual line transitions reveals photoionization as the dominant excitation mechanism (Kinkhabwala et al. 2002; Ogle et al. 2003). The corresponding spectrum obtained with ACIS offers a direct empirical model for the other spectra we discuss here. Figure 7 shows the spectrum from the central $1''.5$ around the nucleus of NGC 1068. It is similar to the others, showing relatively narrow features in the predominantly soft emission, which we fit well with multiple Gaussians.

We measure more emission lines significantly in this high-quality spectrum compared with the other sample members, and we note that much of the flux at energies above 2 keV is in lines, not continuum (Table 7). Young et al. (2001) analyze a spectrum extracted over a slightly larger ($1''.9$) aperture in these same data. They show that the narrow line emission is significant, even when strong soft continuum components are included in the model. While interpretation of the physical nature of X-rays observed at low resolution does depend on the model-fitting procedure, we emphasize that high quality CCD spectra are sufficient to distinguish the thermal or radiative origin of the emission.

Successful models of X-ray spectra of photoionized line emission exist, but we do not attempt to apply a more realistic model to these data for two reasons. First, although emission line ratios are useful diagnostics of physical conditions, including identification of photoionized and collisionally-excited plasmas, we cannot measure any isolated lines in these data to distinguish among competing model descriptions. Second, the models are sensitive primarily to the ionization parameter, the ratio of radiative flux to gas density, given the ionizing spectrum and distribution of illuminated material. In the centers of active galaxies, however, no single ionization parameter is appropriate. In such an inhomogeneous region, individual clumps of gas may have different densities or be located at different distances from the ionizing source, resulting in a range of ionization parameters. In fact, high-quality observations explicitly show a variety of ionization parameters within individual astronomical sources, with each line produced predominantly in the region in which its emissivity is a maximum (e.g., Sako et al. 1999).

5.3. Relationship of Soft X-rays and Continuum Emission

One important result of the spectral fitting is that the soft X-ray emission of the nuclear and central regions consists almost entirely of lines. The soft X-ray emission of many Seyfert 2 galaxies has been attributed to the AGN continuum (e.g., Reichert et al. 1985; Awaki et al. 2000; Matsumoto et al. 2004). In this interpretation, although the central engine is generally obscured, the continuum could be observed through gaps in the covering

material. Alternatively, analogous to the broad emission lines that are sometimes observed in scattered (polarized) light, the obscured AGN continuum could be scattered into the line of sight. These partial covering or scattered continuum models for the soft X-ray emission were generally plausible in the past, given the capabilities of existing instruments. Viewed at low spectral resolution, lines appear blended into a pseudo-continuum, as others have noted while employing continuum models as phenomenological descriptions of their data (e.g., Turner et al. 1997). However, the physical interpretation of these models—in terms of covering fractions and scattering efficiencies, for example—will generate misleading conclusions if fundamentally lines comprise the modeled continuum.

While all galaxies we analyze here exhibit strong soft X-ray emission, it is not the AGN continuum viewed in reflection or through patchy obscuration. Only the central spectrum of ESO 428-G14 includes such a scattered continuum component in the best-fitting model, and it accounts for less than one-third of the 0.5–2 keV flux. We consider the possible contribution of a scattered continuum component to the soft flux of all the nuclear spectra. We find strict upper limits of 10% in NGC 1068 and NGC 1386, 20% in NGC 3393 and NGC 7212, and 26% in the nucleus of ESO 428-G14. Only the lower-quality spectrum of NGC 5347 does not provide a strong limit, allowing up to 60% of the soft flux to be scattered continuum if all the emission lines are much weaker than we find in best-fitting model. High-resolution spectroscopy of comparable AGNs yields similar results. For example, Kinkhabwala et al. (2002) detect no electron-scattered continuum in NGC 1068. The observed soft continuum of the Circinus galaxy accounts for less than 30% of the total 0.5–2 keV flux that includes well-measured lines in addition to the continuum (Sambruna et al. 2001). In Mrk 3, the continuum contributes less than 25% to the observed soft *Chandra* spectrum (Sako et al. 2000), although Bianchi et al. (2005) indicate that the continuum accounts for over 50% of this galaxy’s flux detected with the Reflection Grating Spectrometer of *XMM-Newton* up to 1.5 keV, where the line emission is measured well.

In general, the scattered continuum contribution relative to the intrinsic emission increases with decreased clumping factor and increased ionization parameter (Krolik & Kriss 1995). As these authors demonstrate, scattering can also substantially enhance line emission. This effect is strongest for the resonance transitions, where the line scattered fraction can be a few times the average (continuum) scattered fraction. Resonance lines are most evident in the observed spectra, so scattering as well as direct recombination likely contributes to these features.

We recognize that partial covering models may provide an accurate physical description of some other AGNs. The spectrum of NGC 4151, for example, has been interpreted in this context (Weaver et al. 1994; Ogle et al. 2000). Typically, the “obscured” sources in which the

nucleus appears partially covered at X-ray energies (e.g., Weaver et al. 1996; Immler et al. 2003) exhibit at least some broad optical emission lines (classified as Seyfert types 1.5–1.9). The broad emission lines, which originate close to the central engine, are therefore not fully hidden from direct view. Provided that the covering fraction of the the broad emission line region itself is less than 1, partial unobscured views of the nuclear continuum are possible.

Obscured active galaxies generally display soft X-ray emission greater than that of the absorbed AGN continuum. With their continua fully suppressed, these Compton thick AGNs show that the luminosity of photoionized line emission can be significant, and we suggest that it may contribute to such “soft excesses,” in both obscured and unobscured galaxies. The 0.5–2 keV luminosity of the concentrated central regions is $0.3\text{--}11 \times 10^{40} \text{ erg s}^{-1}$, and the soft luminosity of the entire galaxies ranges from 0.4 to $14 \times 10^{40} \text{ erg s}^{-1}$. These values are comparable to the soft excess luminosity measured in other Seyfert galaxies (e.g., Turner et al. 1997), or the total soft X-ray luminosity of galaxies in which all the direct AGN emission is suppressed below 2 keV, i.e., where $N_H > 10^{23} \text{ cm}^{-2}$ (Guainazzi et al. 2005b).

The soft X-ray emission of the Compton thick AGNs we investigate here is not related in a simple way to their observed or intrinsic hard X-ray emission. The observed nuclear soft flux ranges from 0.1 to 1 times the observed hard X-ray flux, and the ratio of soft to hard flux in the central regions ranges from 0.1 to 0.8. Assuming the buried AGN generates the soft X-ray lines via photoionization, the ratio of observed soft to intrinsic hard emission indicates a reprocessing efficiency. This ratio varies from $1\text{--}3 \times 10^{-3}$, relative to the Fe line estimate of $L_{AGN,2-10}$. The production of soft X-rays through photoionization depends strongly on the properties of the surrounding material that may be illuminated, notably the optical depth and covering fraction. In NGC 5347, for example, the lack of dense material along direct lines of sight to the nucleus is likely responsible for the low reprocessing efficiency.

5.4. A Diagnostic Diagram for Obscured AGN

With limited data, such as in surveys, the observed ratio of soft and hard fluxes in the form of an X-ray hardness ratio is commonly employed to identify an AGN and to determine both the degree of obscuration and the intrinsic luminosity. The hardness ratio is an appropriate measurement if the buried AGN dominates the total X-ray emission and is detected directly in the hard X-ray bandpass. In such instances, the lack of soft X-ray emission accurately indicates the absorption while allowing direct measurement of the true AGN power at higher energies. In these Compton thick galaxies, however, the AGN is not observed directly, and the strong soft X-ray emission is not the AGN continuum. For example, defining the soft band flux (S) from 0.5 to 2 keV and the hard band flux (H) from

2 to 8 keV, the hardness ratio is $(H - S)/(H + S)$. *Evaluating the hardness ratio in the observed nuclear or galaxy spectra would incorrectly indicate that these are unabsorbed and intrinsically weak AGNs*, having $N_H < 2 \times 10^{22} \text{ cm}^{-2}$ and intrinsic $L_{2-10} < 2 \times 10^{41} \text{ erg s}^{-1}$. Figure 8 illustrates the agreement between the observed luminosity ratios and that of an *unobscured* AGN.

The lack of moderate-energy (2–5 keV) photons in the presence of strong soft X-rays distinguishes the heavily obscured AGNs from weakly-absorbed yet genuinely faint sources. When the data do not allow spectral modeling, X-ray “colors” based on intensity ratios in at least three bands would help to identify these sources. Guainazzi et al. (2005b), for example, consider the effect of redshift and utilize a very soft (0.2–0.5 keV) band in their analysis. Alternatively, Levenson et al. (2005) demonstrate that large column densities can be identified when gas heated by stellar winds and supernovae produces the soft X-rays that contaminate the standard hardness ratio. We construct a similar grid of AGN models combined with with varying amounts of photoionization to explore the X-ray colors in soft (0.5–2 keV), medium (2–5 keV), and hard (5–8 keV) bands. We model the AGN continuum as either a $\Gamma = 1.9$ power law absorbed by $0\text{--}10^{24} \text{ cm}^{-2}$ or the pure reflection continuum absorbed by 10^{20} cm^{-2} (for typical Galactic absorption). We separately consider including with the reflection model the flux of an Fe K α line of EW= 1 keV. We adopt the empirical soft line spectrum of ESO 428-G14 to represent the photoionized contribution. We mix the photoionized component with the various AGN models, scaling it to account for 0 to 100% of the total observed counts with each continuum model. Finally, for all summed models, we compute the ratio of counts in the three bands *Chandra* would detect.

Figure 9 shows the model intensity ratios as a “color-color” plot. The results can be ambiguous when the photoionized component accounts for a significant fraction of the total counts. In particular, three-band ratios alone do not distinguish between the pure reflection model of the hard X-ray continuum and moderate absorption ($N_H \approx 1\text{--}3 \times 10^{23} \text{ cm}^{-2}$). With a significant fraction of photoionized counts in these Compton thin spectra, however, the photoionization efficiency is unrealistically large. For $N_H = 10^{23} \text{ cm}^{-2}$, a 50% photoionization contribution (by counts) requires that 6.5% of the intrinsic AGN’s 2–10 keV luminosity emerge in lines in the 0.5–2 keV band. For $3 \times 10^{23} \text{ cm}^{-2}$, the corresponding luminosity fraction is 2.1%. In contrast, we observe a photoionized soft X-ray luminosity $L_{photo,0.5-2} \leq 0.005 L_{AGN,2-10}$ in the high-quality spectra of the Compton thick galaxies of this study. We therefore suggest imposing an upper limit on the allowed photoionization efficiency. With the requirement $L_{photo,0.5-2}/L_{AGN,2-10} \leq 0.01$, the photoionized count fraction is restricted to be less than 14 and 33% for $N_H = 1$ and $3 \times 10^{23} \text{ cm}^{-2}$, respectively. Equivalently, this constraint rules out soft/medium count ratios above 0.2 and 0.9 in these two Compton thin cases. We conclusively identify Compton thick galaxies with a strict limit

of $L_{photo,0.5-2}/L_{AGN,2-10} \geq 0.03$, the area to the right of the thick solid line in Figure 9. These excluded Compton thin mixed models are also marked in red. The model count ratios where $0.01 < L_{photo,0.5-2}/L_{AGN,2-10} < 0.03$ are plotted in green.

Figure 9 also shows the observed *Chandra* count ratios of the nuclei of this study. The simplified approach does not reproduce the results of spectral modeling in detail, but all these AGNs would certainly be recognized as Compton thick. For example, NGC 1386 and NGC 3393 are somewhat weaker in the medium band than the template line emission, so their colors are offset from those of the reflection model. In addition, we plot the observed colors of several contrasting Compton thin galaxies, selected from the available *Chandra* archive and not classified as the obscured counterparts of narrow-line Seyfert 1 galaxies, which may have unusual soft X-ray properties (Leighly 1999). The emission from NGC 5728 was measured within a $2''$ radius aperture. The bright nuclei of NGC 2110, NGC 5252, and NGC 7172 are strongly piled up, so we calculated the count ratios in the resulting readout streak, which remains spectrally accurate. In the three-color diagram, all these contrasting galaxies would be classified as Compton thin, although none of their count ratios lie close to the values of the single-component absorbed power law model (at the extreme left of the solid curves). Finally, we plot the colors of the comparison Compton thick galaxies that also contain nuclear starbursts. Because the X-ray emission of the starbursts is almost entirely soft, the active nuclei in these composite galaxies remain correctly classified as Compton thick. We conclude that the combination of the three X-ray spectral bands and a realistic constraint on the efficiency can identify Compton thick sources without complete spectral modeling.

6. Continuum Reflection Geometry

The relationship between the observable reflected AGN continuum and the intrinsic emission is a function of geometry. Figure 10 schematically illustrates two scenarios that result in reflection-dominated spectra, assuming toroidal distribution of obscuring material around the central engine. The intrinsic AGN light (solid lines) may be reflected off the far side of the torus and then viewed without obscuration (dotted line). Alternatively, the (near-side) obscuring material may simultaneously serve as the reflecting medium, in which case the reflected spectrum (dashed line) is also absorbed, by an amount that depends on the depth within the material at which it is produced. In either case, both the heavily-absorbed intrinsic emission transmitted through the obscurer and the reflected component contribute to the net observed spectrum, but the transmitted component is weak in the Compton thick sources. For simplicity, the cartoon shows a uniform obscurer, although more realistically,

the torus may be inhomogeneous. A clumpy torus results in the same X-ray spectra, provided that the total obscuration along the line of sight is unchanged and—in the first scenario—individual clumps remain optically thick to act as reflectors. (Indeed, rapid X-ray variability observed in other obscured AGNs, such as NGC 1365 (Risaliti et al. 2005), supports the suggestion of a non-uniform torus.) The cartoon also shows the soft X-ray emitting region, which has an unimpeded view of the AGN continuum.

Unlike less-obscured examples, in which some portion of the AGN emission is observed directly, recovering the AGN luminosity from the modeled continuum of these Compton thick galaxies does not yield certain results. Interpreting the model fits to the spectra in terms of either of these scenarios yields a lower limit on $L_{AGN,2-10}$. In the context of the first scenario, we assume the ratio of reflected to intrinsic emission is 1, then compute the 2–10 keV luminosity of the unseen (buried) continuum source. The resulting values of $L_{AGN,2-10}$ are listed in Table 6 (column 6, labeled $L_{AGN,PEX}$). Because the relative reflection is in fact less than 1, with some covering fraction less than 100% by necessity allowing direct views of the reflected continuum, this method gives a lower limit on $L_{AGN,2-10}$.

This estimate of $L_{AGN,2-10}$ is also a lower limit if the second scenario is applicable. As in the first situation, the covering fraction of reflecting material may be less than 1. The reflected spectrum may further be obscured by the foreground layers of the torus. Viewed through a screen of $N_H = 10^{24} \text{ cm}^{-2}$, for example, the emerging flux at 8 keV is reduced by a factor of about 5. Indeed, the values of $L_{AGN,2-10}$ based on the continuum modeling are about an order of magnitude lower than the reasonable estimates we derived from the Fe line luminosities (§5.1), with the exception of NGC 7212. Similar reflected and absorbed descriptions of the observed X-ray emission of obscured AGNs have been proposed previously. Awaki et al. (2000), for example, applied such corrections to a sample of Seyfert 2s and increased the estimated intrinsic hard X-ray luminosity by factors of up to 10 over a single foreground absorber model.

The reflected soft X-ray emission is detectable in the first case, while it is absorbed in the second case. The photoelectric cutoff energy (below which the continuum does not emerge) is a function of the overlying column density, and a cutoff at high energy (indicating large column density) would arise only in the second scenario. While the resulting AGN spectra differ, we cannot discriminate between these situations in the data. Line emission obviously dominates the very soft X-ray spectra, so the presence or absence of the soft reflected continuum is uncertain. At higher energy, where the spectral cutoff could decidedly identify the second scenario, the limited resolution and sensitivity prevent distinction of a true continuum from blended lines.

As long as some portion of the far side of the torus is visible without obscuration,

however, this reflected light dominates the observed hard emission. This first scenario is more important even when the viewing angle is significantly greater than the torus opening half-angle. For example, with a viewing angle $i = 70^\circ$ and $\theta = 40^\circ$, the 8 keV flux of the far-side reflection is nearly an order of magnitude greater than the emerging near-side reflection. In the present data, the existence of the photoionized regions demonstrates that the covering fractions of the tori are less than 1, so the first scenario best describes the origin of the observed reflection spectra.

7. Multiwavelength Comparisons

While deeply buried, the active nucleus remains the primary energy source in each of these galaxies. We compare the X-ray results with several other indicators of the luminosity of these very obscured AGNs at other wavelengths. Much of the intrinsic luminosity emerges at IR wavelengths, but stellar emission is a source of confusion. The extreme ultraviolet (EUV) dominates the intrinsic spectral energy distribution (SED), and we probe this regime indirectly through optical recombination lines. We demonstrate that the intrinsic properties of these AGNs are similar to their less obscured and unobscured counterparts. However, their observable characteristics are distinct, and therefore offer some identifying signatures.

These Compton thick galaxies generally exhibit 25- to 60- μm flux ratios typical of AGNs ($f_{25}/f_{60} > 0.26$; de Grijp et al. 1987), in contrast to cooler, stellar-heated dust. We calculate the total 8–1000 μm infrared luminosity from *IRAS* fluxes, following the prescription of Sanders & Mirabel (1996), and find $L_{IR} \sim 10^{43}$ erg s $^{-1}$ (Table 6). The total IR luminosity indicates the bolometric luminosity; in unobscured quasars, $L_{bol} \approx 5L_{IR}$. Ignoring any stellar contributions and applying this relationship to these Compton thick sources suggests $L_{bol} \sim 10^{44}$ – 10^{45} erg s $^{-1}$ here.

While the ratio of directly-observed X-ray to L_{IR} is very low for AGNs, with $L_{obs,2-10}/L_{IR} < 10^{-3}$ in all cases, considering the intrinsic X-ray luminosity, $L_{AGN,Fe}/L_{IR} \sim 0.1$. These latter flux ratios are similar to those measured in unobscured sources. For example, in the median radio-quiet quasar spectrum of Elvis et al. (1994), $L_{AGN,2-10}/L_{IR} = 0.2$. Risaliti & Elvis (2004) derive the average quasar SED in several broad bands, including corrections for sample selection effects. This average spectrum has $L_{AGN,2-10}/L_{IR} = 0.05$ – 0.2 , depending somewhat on the assumed hard X-ray spectral shape and treatment of the shortest-wavelength IR emission.

Neither the composite SEDs nor our AGNs have been corrected for star-heated dust emission at IR wavelengths, which can be important within the large *IRAS* apertures. For

example, while the kpc-scale star-forming ring of NGC 1068 is easily excluded from the nuclear X-ray measurements, it does contribute significantly to the IR measurements. The comparison of this sample with active galaxies that also exhibit significant star formation demonstrates that L_{IR} is not a reliable indicator of intrinsic AGN luminosity when the stellar populations are unknown. While the correlations of IR luminosity with AGN indicators based on [O III] and Fe line luminosity are similar for the non-starburst Compton thick AGNs and unobscured AGNs, the active galaxies that also contain strong star formation show IR luminosities that are up to an order of magnitude higher (Figure 11).

Mid-infrared emission requires hotter dust, so the stellar contribution to the integrated luminosity is proportionally smaller in this restricted wavelength range (8–40 μ m). As Figure 12 illustrates, however, even the mid-IR excess of the star-forming galaxies is significant. Similar to Figure 11, the non-starburst Compton thick galaxies exhibit luminosity ratios comparable to those of unobscured AGNs. Although the mid-IR does not always dominate the total IR luminosity, the two are very well-correlated in non-starburst galaxies because the underlying energy source—the AGN—is the same.

The large-scale optical emission provides one more method for constraining the intrinsic luminosity of these AGNs. The recombination rate of hydrogen is related to the H α line luminosity $N_{rec} = 7.4 \times 10^{11} L_{H\alpha}$, where $L_{H\alpha}$ is measured in erg s $^{-1}$ (Mulchaey et al. 1994). Assuming every hydrogen-ionizing photon that encounters circumnuclear material eventually results in recombination, the ratio of the recombination rate to the total ionization rate is the covering fraction, C , of photoionized material. We assume a power-law spectrum from the optical to X-ray bandpass, $L_\nu \propto \nu^{-\alpha}$, with $\alpha = 1.5$. Integrating this continuum from the hydrogen ionization edge through 2 keV, the ionizing luminosity $L_{ion} \propto L_{H\alpha} C^{-1}$.

We measure $L_{H\alpha}$ and C from the continuum-subtracted *HST* image of ESO 428-G14. In the resulting image, we find that line emission extends over the $3''.5 \times 1''.1$ region around the nucleus, for $C = 0.20$. We use the WFPC2 exposure time calculator⁷ to convert the observed count rate to flux for the line spectrum. We correct for the [N II] emission which accounts for about 1/3 of the flux in the filter bandpass here (Falcke et al. 1996). We also correct for the Galactic extinction to yield $F_{H\alpha} = 8.1 \times 10^{-13}$ erg cm $^{-2}$ s $^{-1}$.

Ferruit, Wilson, & Mulchaey (2000) report a flux of 5.4×10^{-13} erg cm $^{-2}$ s $^{-1}$ from H α and [N II] in a $6'' \times 8''$ aperture at the center of NGC 1386. Because this measurement was made through *HST*'s linear ramp filter, the sensitivity to the [N II] doublet is less than that of H α . We do not correct for the [N II] contamination here. We measure the covering fraction of the extended H α emission in the PC image, finding $C = 0.17$. Cooke

⁷http://www.stsci.edu/instruments/wfpc2/Wfpc2_etc/wfpc2-etc.html

et al. (2000) report a flux of $3.67 \times 10^{-13} \text{ erg cm}^{-2} \text{ s}^{-1}$ from $H\alpha$ and [N II] in a $7''.5 \times 12''.4$ area around the nucleus of NGC 3393. Correcting for Galactic extinction and an estimated 33% contamination of [N II], $F_{H\alpha} = 4.4 \times 10^{-13} \text{ erg cm}^{-2} \text{ s}^{-1}$. We measure the covering fraction of the S-shape evident in the *HST* continuum image, which line emission dominates, and find $C = 0.26$. We determine the covering fraction of NGC 5347 in the continuum-subtracted [O III] image from *HST* (Schmitt et al. 2003). Measuring the opening angle to the northeastern emission, we find $C = 0.22$. In narrow-band images, González Delgado & Perez (1996) find $F_{H\alpha} = 7.1 \times 10^{-13} \text{ erg cm}^{-2} \text{ s}^{-1}$ from the nucleus and northeastern knot together, after correcting for [N II] emission and extinction.

Table 6 lists $L_{H\alpha}$ and the calculated values of L_{ion} ; the latter are generally around $10^{43} \text{ erg s}^{-1}$, except for the lower-luminosity NGC 1386. This method of calculating L_{ion} yields a lower limit on the true value. The large-scale geometry of the emission-line region determines the value of C . Because the gas is clumpy on small scales, however, the true covering factor could be substantially smaller, resulting in larger values of L_{ion} . Also, while we correct the line fluxes for Galactic extinction, we do not correct for intrinsic dust absorption.

We associate the X-ray photoionized material with the optical narrow line region. The observed line luminosity $L_{H\alpha}$ is typically an order of magnitude larger than the total observed 0.5–2 keV luminosity. The total luminosity of the narrow line region in optical and UV lines is then a few $\times 10^{42}$ to $10^{43} \text{ erg s}^{-1}$, or several orders of magnitude greater, even without correcting for intrinsic extinction or covering fraction. Fundamentally, these luminosity differences demonstrate that the emission region is optically thin to X-rays but optically thick in the extreme ultraviolet (EUV), the ionizing continuum of the optical lines.

Another way to quantify this difference is in terms of the emission measure, $EM = \int n^2 dl$, where n is density, integrated along the line of sight. We treat all of the emission in the X-ray “lines” near 0.56 and 0.91 keV as O VII and Ne IX, respectively, using the maximum line emissivities from the XSTAR photoionization code (Kallman & Bautista 2001). Table 8 lists the emission measures, evaluating over the central regions of ESO 428-G14, NGC 1386, and NGC 3393, and the nucleus of NGC 5347. We use the $H\alpha$ areas and luminosities above to find $EM_{H\alpha}$. The X-ray emission measures are generally several orders of magnitude smaller than the corresponding $EM_{H\alpha}$, even though we overestimate all the X-ray line fluxes by counting blends of many unresolved lines. The $H\alpha$ emission measure of NGC 3393 is relatively low, a consequence of the very large area ($7''.5 \times 12''.4$) over which the luminosity was measured, while the bright $H\alpha$ emission is confined to a much smaller area ($2'' \times 4''$).

The viewing geometry of these Seyfert galaxies reveals the X-ray line emission and optical narrow line regions directly, and these may be related to the “warm absorbers” and

UV absorbers observed in unobscured AGNs (Blustin et al. 2005; Crenshaw et al. 2003). The present observations and known warm absorbers are different in several ways, however. First, the X-ray emission measures indicate somewhat lower column densities (e.g., $N_{OVII} \sim 10^{18}$ rather than 10^{19} cm^{-2}), although these are uncertain by an order of magnitude, given the unknown covering fractions. Second, the lower ionization states, such as O VII and Ne IX, are the most prominent emission features here. (High resolution spectra reveal some emission from fully-ionized species, but it tends to be weaker and have smaller emission measure; Sako et al. 2000; Kinkhabwala et al. 2002.) In contrast, fully-ionized species predominate in the absorption spectra (e.g., Netzer et al. 2003; Yaqoob et al. 2003). Finally, the spatial scales of the emission and absorption appear to be different. While we measure emission on scales of hundreds of pc, UV and X-ray absorbers are located within tens of pc of the AGN (Crenshaw & Kraemer 2005, and references therein). Although they are not identical, the absorbing and emitting material need not have entirely distinct origins to account for these observed differences. Instead, each preferentially samples a common distribution of properties differently: “warm absorption” spectra reveal the smaller scale, rapidly outflowing material, while the material located farther from the nuclei dominates emission.

The multiwavelength data overall answer two important questions: How is the bolometric luminosity of the AGNs distributed across the electromagnetic spectrum, and at which energies are the active nuclei revealed? Most of the luminosity clearly emerges in the IR. The IR spectra and near-constancy of intrinsic X-ray to IR luminosity ratios demonstrate that the buried AGNs produce the observed IR emission in these galaxies lacking starbursts. With our calculation of L_{ion} , we indirectly recover most but not all of the intrinsic EUV luminosity. The AGNs themselves preferentially emit in the EUV, and this is the dominant bandpass of quasar spectral energy distributions (Elvis et al. 1994), although the emergent EUV radiation of all obscured AGNs, even the Compton thin variety, is weak. Indeed, we find rough agreement between L_{ion} and L_{IR} as estimates of the bolometric luminosity of each of the buried AGNs. The sense of the discrepancy between the two wavelength regimes ($L_{ion} < L_{IR}$) is expected, for the calculated L_{ion} is a lower limit and the observed L_{IR} may be contaminated by star-heated sources in the large aperture. We conclude that the underlying spectra of these Compton thick AGNs are similar to those of unobscured sources, although the observable spectra are very different.

The AGN characteristics of Compton thick sources are not different from other obscured AGNs at optical wavelengths, so there is no special bias against finding them in surveys. The general disadvantages of optical identification of Seyfert 2s are relevant, particularly the necessity of obtaining spectra rather than images alone, and host galaxy dilution of the AGN spectral features, which becomes more severe at high redshift (Moran, Filippenko, & Chornock 2002).

X-ray surveys efficiently find active galaxies, despite the small fraction ($\lesssim 5\%$) of the total luminosity even unobscured AGNs emit in this bandpass. The high sensitivity of the current detectors and the high contrast with stellar sources (which are proportionately even fainter in X-rays) particularly contribute to this success. The Compton thick examples here, however, illustrate the types of sources that X-ray surveys can miss.

X-ray observations with even modest spectral resolution do offer one technique to identify Compton thick AGNs specifically: the large EW of Fe $K\alpha$, as we and others have previously suggested (Levenson et al. 2002; Maccacaro et al. 2004). Measuring the line against the suppressed continuum does not require complex spectral modeling. The line emission is confined to a narrow spectral bandpass, so the desired signal may easily stand out against the low background of *Chandra* and *XMM-Newton* within a limited energy range. Furthermore, with the EW as a constraint, the line luminosity is an effective indicator of the intrinsic AGN luminosity.

Compton thick AGNs may reveal themselves in the IR, having long-wavelength spectral slopes similar to other types of AGNs. An important caveat for IR identification, however, is that the AGNs do not always dominate the IR emission, even at mid-IR wavelengths. Starbursts can be powerful, resulting in IR spectra that do not indicate the active nuclei that are present. Such stellar contamination is a real concern, because starbursts are common in active galaxies.

The Compton thick AGNs themselves may be viewed directly only at high energy ($E > 10$ keV), yet even then obscuration in excess of $10^{25.5} \text{ cm}^{-2}$ can reduce the emergent high-energy flux by two orders of magnitude. Provided the obscuration is not so severe, the SWIFT Burst Alert Telescope survey should detect Seyfert galaxies like these and provide direct measurements of the intrinsic AGN luminosities. The limiting 15–150 keV flux of the survey will be 1 mCrab after two years of operation (Parsons et al. 2004). Using the Fe line-determined $L_{AGN,2-10}$ to predict the harder emission, these sources have flux around 2–3 mCrab. Other bright Seyfert galaxies with intrinsic $L_{AGN,2-10} = 10^{43} \text{ erg s}^{-1}$ could be detected to a distance of nearly 80 Mpc. Truly luminous obscured AGN having X-ray luminosities two orders of magnitude greater would be detectable to nearly $z = 0.2$.

8. Conclusions

Nearby Seyfert galaxies serve as important examples of AGNs in general and Compton thick sources specifically. Because stellar sources do not significantly contaminate the X-ray emission and the direct AGN light is blocked, the present observations sensitively reveal

the variety of X-rays that AGNs alone can produce. While the underlying continuum may be a simple power law, the radiation that emerges is reprocessed, in soft photoionized lines and a weakened hard continuum. We find no evidence here that the soft X-ray emission is primarily the AGN continuum viewed through patchy obscuration or scattered into the line of sight. When active nuclei are viewed directly, as in type 1 sources, the powerful continuum dominates the entire observed spectrum. With the direct soft X-rays blocked, however, even by smaller column densities than in these examples, the detectable soft X-rays may be in emission lines.

These spectra clearly show that line emission, not a smooth continuum, composes the soft X-ray spectrum. Although we do not spectrally resolve individual transitions, the present resolution is sufficient to identify photoionization as opposed to collisional excitation as the origin of the line emission. In all cases, the correlation of the extended soft X-rays with photoionized line emission at optical wavelengths supports this interpretation.

Because the observed soft X-ray emission is not the AGN continuum viewed directly, the commonly-employed hardness ratio does not accurately measure either the obscuration or the intrinsic luminosity of these sources. Instead, we propose a three-“color” diagnostic to characterize AGNs—including the Compton thick ones—when high-quality data are not available for spectroscopy.

Typical of Compton thick AGNs, even the hard X-rays that Chandra detects here are reflected, being only about 1% of the intrinsic AGN power. The clearest X-ray signature of the active nucleus in each of these galaxies is the large EW Fe K α line emission, with EW > 1 keV in all cases. The EWs are large because the line is measured against a reflected continuum.

We determine the intrinsic luminosity several ways. The most reliable method in these data comes from the Fe line luminosity. The hidden emission emerges in the IR, and the intrinsic X-ray/IR flux ratios are typical of unobscured quasars, except where stellar IR contributions are strong. Because star-heated dust may be luminous, even at mid-IR wavelengths, IR data alone do not accurately measure the AGN luminosity. The X-ray continuum modeling provides only a lower limit on the AGN luminosity, independent of the assumed reflection geometry. The reflection fraction is unknown, and the reflector may itself be obscured.

This research has made use of the NASA/IPAC Extragalactic Database (NED) which is operated by the Jet Propulsion Laboratory, California Institute of Technology, under contract with the National Aeronautics and Space Administration, and it has made use of data obtained from the High Energy Astrophysics Science Archive Research Center (HEASARC),

provided by NASA’s Goddard Space Flight Center. Some of the data presented in this paper were obtained from the Multimission Archive at the Space Telescope Science Institute (MAST). STScI is operated by the Association of Universities for Research in Astronomy, Inc., under NASA contract NAS5-26555. This work was supported by NASA through grant GO4-5117 and NSF award AST-0237291. NAL thanks the GSFC X-ray Astrophysics Laboratory for their hospitality and the NSFRO for support during part of this work.

Facilities: BeppoSAX (PDS), CXO (ACIS), HST (WFPC2)

A. Additional Sources

In the *Chandra* images, we identify a number of sources in addition to the AGNs within $2'$ of each galaxy’s center. The sources are detected with a minimum of 3 net counts and non-zero spatial extent using the CIAO wavdetect algorithm. We considered total (0.3–8 keV), low-energy (0.3–2 keV) and high-energy (4–8 keV) images separately, but the sources of the latter two images are a subset of sources in the total-band image. In all cases, we measure the counts in a $3''$ radius aperture after subtracting a local background. The source locations and their net count rates are listed in Table 9. The table also contains the projected angular distance of each source from the nucleus of the Compton thick galaxy in the field and the corresponding physical scale at the distance of the central galaxy.

We very crudely estimate the observed fluxes of these sources, assuming that their spectra are power laws with $\Gamma = 1.9$, absorbed by the Galactic foreground column density. We find that $1 \times 10^{-4} \text{ count s}^{-1}$ corresponds to $8 \times 10^{-16} \text{ erg cm}^{-2} \text{ s}^{-1}$. Individual sources with total X-ray luminosity $> 10^{39} \text{ erg s}^{-1}$ are of interest as “ultraluminous X-ray” candidates (Miller & Colbert 2004). This limit corresponds to observed count rates of 17, 67, 4, 10, and $0.8 \times 10^{-4} \text{ counts s}^{-1}$ in ESO 428-G14, NGC 1386, NGC 3393, NGC 5347, and NGC 7212, respectively, assuming the sources are located in the host galaxy. However, the large apertures in which the source counts are measured here encompass hundreds of parsecs and therefore likely include many distinct sources.

These additional sources may be entirely independent of the galaxies at the centers of these fields. The sources around ESO 428-G14 and NGC 1386 tend to be soft, however, and the number of sources in each of these region exceeds the source count rates of blank sky fields. Applying the results of Tozzi et al. (2001), for example, we would expect fewer than about 5 sources with 0.5–2 keV count rates $> 1 \times 10^{-4} \text{ count s}^{-1}$ in each of the $13\Gamma'$ areas we surveyed, while we find 17 and 13 around ESO 428-G14 and NGC 1386, respectively. These facts suggest that many of the sources are indeed associated with (and possibly located in)

these host galaxies. Because the total number of sources is small, there is no significant trend in the number of sources as a function of distance from the center of each galaxy. The number of sources we find near NGC 3393, NGC 5347, and NGC 7212 is not significantly greater than the detection rates expected from blank field observations. We do measure soft emission from all of the additional sources near NGC 3393 and NGC 7212, and from half the sources near NGC 5347.

REFERENCES

- Anders, E., & Grevesse, N. 1989, *Geochim. Cosmochim. Acta*, 53, 197
- Antonucci, R. 1993, *ARA&A*, 31, 473
- Arnaud, K. A. 1996, in ASP Conf. Ser. 101, *Astronomical Data Analysis Software and Systems V*, ed. G. Jacoby & J. Barnes (San Francisco: ASP), 17
- Awaki, H., Koyama, K., Inoue, H., & Halpern, J. P. 1991, *PASJ*, 43, 195
- Awaki, H., Ueno, S., Taniguchi, Y., & Weaver, K. A. 2000, *ApJ*, 542, 175
- Bergvall, N., Johansson, L., & Olofsson, K. 1986, *A&A*, 166, 92
- Bianchi, S., Guainazzi, M., & Chiaberge, M. 2006, *A&A*, 448, 499
- Bianchi, S., Miniutti, G., Fabian, A. C., & Iwasawa, K. 2005, *MNRAS*, 360, 380
- Blustin, A. J., Page, M. J., Fuerst, S. V., Branduardi-Raymont, G., & Ashton, C. E. 2005, *A&A*, 431, 111
- Cash, W. 1979, *ApJ*, 228, 939
- Cid Fernandes, R., Gu, Q., Melnick, J., Terlevich, E., Terlevich, R., Kunth, D., Rodrigues Lacerda, R., & Joguet, B. 2004, *MNRAS*, 355, 273
- Cid Fernandes, R., Heckman, T., Schmitt, H., Delgado, R. M. G., & Storchi-Bergmann, T. 2001, *ApJ*, 558, 81
- Cid Fernandes, R. J., Storchi-Bergmann, T., & Schmitt, H. 1998, *MNRAS*, 297, 579
- Colbert, E. J. M., Heckman, T. M., Ptak, A. F., Strickland, D. K., & Weaver, K. A. 2004, *ApJ*, 602, 231
- Comastri, A., Setti, G., Zamorani, G., & Hasinger, G. 1995, *A&A*, 296, 1

- Cooke, A. J., Baldwin, J. A., Ferland, G. J., Netzer, H., & Wilson, A. S. 2000, *ApJS*, 129, 517
- Crenshaw, D. M., et al. 2003, *ApJ*, 594, 116
- Crenshaw, D. M., & Kraemer, S. B. 2005, *ApJ*, 625, 680
- de Grijp, M. H. K., Lub, J., & Miley, G. K. 1987, *A&AS*, 70, 95
- Diaz, A. I., Prieto, M. A., & Wamsteker, W. 1988, *A&A*, 195, 53
- Elvis, M., et al. 1994, *ApJS*, 95, 1
- Falcke, H., Wilson, A. S., Simpson, C., & Bower, G. A. 1996, *ApJ*, 470, L31
- Ferruit, P., Wilson, A. S., & Mulchaey, J. 2000, *ApJS*, 128, 139
- Ghisellini, G., Haardt, F., & Matt, G. 1994, *MNRAS*, 267, 743
- González Delgado, R. M., Heckman, T., & Leitherer, C. 2001, *ApJ*, 546, 845
- González Delgado, R. M., & Perez, E. 1996, *MNRAS*, 280, 53
- Guainazzi, M., Fabian, A. C., Iwasawa, K., Matt, G., & Fiore, F. 2005a, *MNRAS*, 356, 295
- Guainazzi, M., Matt, G., & Perola, G. C. 2005b, *A&A*, 444, 119
- Heckman, T. M., Armus, L., & Miley, G. K. 1990 *ApJS*, 74, 833
- Heckman, T. M., Ptak, A., Hornschemeier, A., & Kauffmann, G. 2005, *ApJ*, 634, 161
- Imanishi, M. 2003, *ApJ*, 599, 918
- Immler, S., Brandt, W. N., Vignali, C., Bauer, F. E., Crenshaw, D. M., Feldmeier, J. J., & Kraemer, S. B. 2003, *AJ*, 126, 153
- Kallman, T., & Bautista, M. 2001, *ApJS*, 133, 221
- Kinkhabwala, A. et al. 2002, *ApJ*, 575, 732
- Kinney, A. L., Bohlin, R. C., Calzetti, D., Panagia, N., & Wyse, R. F. G. 1993, *ApJS*, 86, 5
- Kinney, A. L., Calzetti, D., Bohlin, R. C., McQuade, K., Storchi-Bergmann, T., & Schmitt, H. R. 1996, *ApJ*, 467, 38

- Koyama, K., Inoue, H., Tanaka, Y., Awaki, H., Takano, S., Ohashi, T., & Matsuoka, M. 1989, PASJ, 41, 731
- Krolik, J. H., & Kriss, G. A. 1995, ApJ, 447, 512
- Krolik, J. H., Madau, P., & Życki, P. T. 1994, ApJ, 420, L57
- Leighly, K. M. 1999, ApJS, 125, 317
- Levenson, N. A., Krolik, J. H., Życki, P. T., Heckman, T. M., Weaver, K. A., Awaki, H., & Terashima, Y. 2002, ApJ, 573, L81
- Levenson, N. A., Weaver, K. A., Heckman, T. M., Awaki, H., & Terashima, Y. 2004, ApJ, 602, 135
- Levenson, N. A., Weaver, K. A., Heckman, T. M., Awaki, H., & Terashima, Y. 2005, ApJ, 618, 167
- Levenson, N. A., Weaver, K. A., & Heckman, T. M. 2001, ApJS, 133, 269
- Liedahl, D. A., Osterheld, A. L., & Goldstein, W. H. 1995, ApJ, 438, L115
- Maccacaro, T., Braito, V., Della Ceca, R., Severgnini, P., & Caccianiga, A. 2004, ApJ, 617, L33
- Magdziarz, P. & Zdziarski, A. A. 1995, MNRAS, 273, 837
- Maiolino, R., Salvati, M., Bassani, L., Dadina, M., della Ceca, R., Matt, G., Risaliti, G., & Zamorani, G. 1998, A&A, 338, 781
- Marshall, F. E., Boldt, E. A., Holt, S. S., Miller, R. B., Mushotzky, R. F., Rose, L. A., Rothschild, R. E., & Serlemitsos, P. J. 1980, ApJ, 235, 4
- Matsumoto, C., Nava, A., Maddox, L. A., Leighly, K. M., Grupe, D., Awaki, H., & Ueno, S. 2004, ApJ, 617, 930
- Mewe, R., Gronenschild, E. H. B. M., & van den Oord, G. H. J. 1985, A&AS, 62, 197
- Mewe, R., Lemen, J. R., & van den Oord, G. H. J. 1986, A&AS, 65, 511
- Miller, M. C., & Colbert, E. J. M. 2004, Int. J. Mod. Phys. D, 13, 1
- Moran, E. C., Filippenko, A. V., & Chornock, R. 2002, ApJ, 579, L71

- Mulchaey, J. S., Wilson, A. S., Bower, G. A., Heckman, T. M., Krolik, J. H., & Miley, G. K. 1994, *ApJ*, 433, 625
- Nandra, K., & Pounds, K. A. 1994, *MNRAS*, 268, 405
- Netzer, H., et al. 2003, *ApJ*, 599, 933
- Ogle, P. M., Brookings, T., Canizares, C. R., Lee, J. C., & Marshall, H. L. 2003, *A&A*, 402, 849
- Ogle, P. M., Marshall, H. L., Lee, J. C., & Canizares, C. R. 2000, *ApJ*, 545, L81
- Parsons, A. M., et al. 2004, *Proc. SPIE*, 5165, 190
- Reichert, G. A., Mushotzky, R. F., Holt, S. S., & Petre, R. 1985, *ApJ*, 296, 96
- Risaliti, G., & Elvis, M. 2004, *ASSL Vol. 308: Supermassive Black Holes in the Distant Universe*, 187
- Risaliti, G., Elvis, M., Fabbiano, G., Baldi, A., & Zezas, A. 2005, *ApJ*, 623, L93
- Risaliti, G., Gilli, R., Maiolino, R., & Salvati, M. 2000, *A&A*, 357, 13
- Risaliti, G., et al. 1999, *ApJ*, 522, 157
- Sambruna, R. M., Netzer, H., Kaspi, S., Brandt, W. N., Chartas, G., Garmire, G. P., Nousek, J. A., & Weaver, K. A. 2001, *ApJ*, 546, L13
- Sako, M., Kahn, S. M., Paerels, F., & Liedahl, D. A. 2000, *ApJ*, 543, L115
- Sako, M., Liedahl, D. A., Kahn, S. M., & Paerels, F. 1999, *ApJ*, 525, 921
- Sanders, D. B., & Mirabel, I. F. 1996, *ARA&A*, 34, 749
- Schlegel, D. J., Finkbeiner, D. P., & Davis, M. 1998, *ApJ*, 500, 525
- Schmitt, H. R., Donley, J. L., Antonucci, R. R. J., Hutchings, J. B., & Kinney, A. L. 2003, *ApJS*, 148, 327
- Setti, G., & Woltjer, L. 1989, *A&A*, 224, L21
- Strickland, D. K., Heckman, T. M., Weaver, K. A., Hoopes, C. G., & Dahlem, M. 2002, *ApJ*, 568, 689
- Tozzi, P., et al. 2001, *ApJ*, 562, 42

Turner, T. J., George, I. M., Nandra, K., & Mushotzky, R. F. 1997, ApJS, 113, 23

Weaver, K. A., Nousek, J., Yaqoob, T., Mushotzky, R. F., Makino, F., & Otani, C. 1996, ApJ, 458, 160

Weaver, K. A., Yaqoob, T., Holt, S. S., Mushotzky, R. F., Matsuoka, M. & Yamauchi, M. 1994, ApJ, 436, L27

Whittle, M. 1992, ApJS, 79, 49

Worsley, M. A., et al. 2005, MNRAS, 357, 1281

Yaqoob, T., McKernan, B., Kraemer, S. B., Crenshaw, D. M., Gabel, J. R., George, I. M., & Turner, T. J. 2003, ApJ, 582, 105

Young, A. J., Wilson, A. S., & Shopbell, P. L. 2001, ApJ, 556, 6

This preprint was prepared with the AAS L^AT_EX macros v5.2.

Table 1. Observations and Galaxy Data

Galaxy	Observation Date	Exposure (ks)	N_H (cm ⁻²)	z	Distance (Mpc)	scale (pc/'')	RA ^a	Decl ^a
ESO 428-G14	2003 Dec 26	29.6	1.2×10^{21}	0.0057	24.3	120	07 16 31.18	-29 19 28.92
NGC 1068	2000 Feb 22	1.53	2.2×10^{20}	0.0038	16.2	80	02 42 40.69	-00 00 48.11
NGC 1386	2003 Nov 19	19.6	7.7×10^{19}	0.0029	12.4	60	03 36 46.18	-35 59 57.33
NGC 3393	2004 Feb 28	28.0	4.7×10^{20}	0.0125	53.6	260	10 48 23.44	-25 09 43.53
NGC 5347	2004 Jun 05	33.6	1.3×10^{20}	0.0078	33.4	160	13 53 17.80	+33 29 27.40
NGC 7212	2003 Jul 22	19.9	4.5×10^{20}	0.0266	114	550	22 07 02.00	+10 14 01.00
Mrk 3	1.2×10^{21}	0.0135	57.9	280

^aMeasured from peak Fe emission.

Table 2. Hard X-ray Spectral Parameters

Galaxy	E^a_{Fe}	F^b_{Fe}	EW^c_{Fe}	A^d_{AGN}	C/dof
ESO 428-G14	6.35 ± 0.03	7.6 ± 2	1.6 ± 0.5	1.7 ± 0.3	238/270
NGC 1068 ^e	6.42 ± 0.05	51^{+30}_{-20}	1.2 ± 0.7	15 ± 0.5	115/201
NGC 1386	6.39 ± 0.03	5.5^{+2}_{-4}	2.3 ± 1.5	0.8 ± 0.2	173/270
NGC 3393	6.41 ± 0.07	4.2 ± 2	1.4 ± 0.7	$1.0^{+0.3}_{-0.2}$	189/270
NGC 5347	6.38 ± 0.03	4.7 ± 2	1.3 ± 0.5	1.2 ± 0.2	231/270
NGC 7212	6.39 ± 0.04	8.1 ± 3	1.0 ± 0.4	2.7 ± 0.5	277/270

Note. — Errors are 90% confidence limits for one interesting parameter.

^aEnergy of line center in keV.

^bLine flux in 10^{-6} photons $\text{cm}^{-2} \text{s}^{-1}$.

^cEquivalent width of line in keV.

^dNormalization of intrinsic power law in units of 10^{-3} photons $\text{keV}^{-1} \text{cm}^{-2} \text{s}^{-1}$ at 1 keV.

^eFit over 5–8 keV.

Table 3. ESO 428-G14 Soft Spectra

Nucleus		Center	
E^a <i>line</i>	F^b <i>line</i>	E^a <i>line</i>	F^b <i>line</i>
0.61 ± 0.03	23 ± 6	0.58 ± 0.03	26 ± 7
0.77 ± 0.03	20 ± 5	0.77 ± 0.02	23 ± 6
0.91 ± 0.02	18 ± 4	0.90 ± 0.02	25 ± 6
1.07 ± 0.02	11 ± 2	1.06 ± 0.02	13 ± 4
1.23 ± 0.03	4.3 ± 1	1.21 ± 0.04	4.4 ± 2
1.42 ± 0.02	4.4 ± 1	1.41 ± 0.03	4.2 ± 1
1.73 ± 0.03	2.5 ± 0.8	1.75 ± 0.05	1.8 ± 1
1.94 ± 0.04	2.2 ± 0.8	1.88 ± 0.06	2.0 ± 1
2.40 ± 0.04	2.6 ± 1	2.36 ± 0.06	2.6 ± 1
Additional Parameters			
Γ	...	1.9f	
A^c Γ	...	3.0 ± 0.7	
χ^2/dof	25/26	46/49	

Note. — Errors are 90% confidence limits for one interesting parameter. Fixed parameters are marked with f.

^aEnergy of line center in keV.

^bLine flux in 10^{-6} photons $\text{cm}^{-2} \text{s}^{-1}$.

^cNormalization of power law in units of 10^{-5} photons $\text{keV}^{-1} \text{cm}^{-2} \text{s}^{-1}$ at 1 keV.

Table 4. NGC 3393 Soft Spectra

Nucleus		Center	
E^a line	F^b line	E^a line	F^b line
...	...	0.40 ± 0.09	91 ± 60
0.57 ± 0.03	26 ± 7	0.56 ± 0.01	98 ± 20
0.70 ± 0.03	13 ± 5	0.72 ± 0.02	33 ± 6
0.87 ± 0.02	12 ± 3	0.88 ± 0.01	33 ± 5
Additional Parameters			
kT (keV)	1.6 ± 0.3	1.7 ± 0.2	
A^c thermal	3.3 ± 0.7	8.8 ± 1	
χ^2/dof	22/22	68/53	

Note. — Errors are 90% confidence limits for one interesting parameter.

^aEnergy of line center in keV.

^bLine flux in 10^{-6} photons $\text{cm}^{-2} \text{s}^{-1}$.

^cNormalization of thermal component in units of $10^{-5}K$, where $K = (10^{-14}/(4\pi D^2)) \int n_e n_H dV$, D is the distance to the source (cm), n_e is the electron density (cm^{-3}), and n_H is the hydrogen density (cm^{-3}).

Table 5. Observed Flux

Region	$F_{0.5-2}$ (10^{-13} erg cm $^{-2}$ s $^{-1}$)	F_{2-10} (10^{-13} erg cm $^{-2}$ s $^{-1}$)
ESO 428-G14 nucleus	0.91 ± 0.2	3.8 ± 0.5
ESO 428-G14 center	1.4 ± 0.1	4.7 ± 0.5
ESO 428-G14 galaxy	1.7 ± 0.3	6.5 ± 0.7
NGC 1386 nucleus	1.1 ± 0.2	2.1 ± 0.1
NGC 1386 center	1.6 ± 0.2	2.1 ± 0.4
NGC 1386 galaxy	2.2 ± 0.2	3.8 ± 1
NGC 3393 nucleus	0.73 ± 0.07	2.1 ± 0.04
NGC 3393 center	2.0 ± 0.2	2.4 ± 0.07
NGC 3393 galaxy	2.7 ± 0.2	4.2 ± 0.9
NGC 5347 nucleus	0.24 ± 0.04	2.2 ± 0.4
NGC 5347 northeast	0.035 ± 0.01	...
NGC 5347 galaxy	0.34 ± 0.1	2.3 ± 0.3
NGC 7212 nucleus	0.43 ± 0.2	3.9 ± 0.9
NGC 7212 center	0.67 ± 0.3	5.4 ± 0.6
NGC 7212 galaxy	0.92 ± 0.3	6.5 ± 0.7

Table 6. Observed and Intrinsic Luminosity

Galaxy	$L_{obs,0.5-2}^a$	$L_{obs,2-10}^a$	L_{Fe}	$L_{AGN,Fe}^b$	$L_{AGN,PEX}^c$	$L_{AGN,[OIII]}^d$	L_{IR}^e	$L_{H\alpha}$	L_{ion}^f
ESO 428-G14	6.6×10^{39}	2.3×10^{40}	5.5×10^{39}	3.0×10^{42}	3.6×10^{41}	7.6×10^{42}	4.1×10^{43}	5.7×10^{40}	1.3×10^{43}
NGC 1068	1.3×10^{41}	1.1×10^{41}	1.6×10^{40}	7.7×10^{42}	6.3×10^{41}	2.5×10^{43}	1.0×10^{45}
NGC 1386	2.0×10^{39}	3.9×10^{39}	1.1×10^{39}	6.6×10^{41}	5.2×10^{40}	5.8×10^{41}	1.3×10^{43}	1.0×10^{40}	2.6×10^{42}
NGC 3393	2.3×10^{40}	7.5×10^{40}	1.5×10^{40}	7.2×10^{42}	1.0×10^{42}	1.7×10^{43}	9.6×10^{43}	1.5×10^{41}	2.6×10^{43}
NGC 5347	3.2×10^{39}	3.0×10^{40}	6.4×10^{39}	3.0×10^{42}	4.8×10^{41}	6.5×10^{42}	3.7×10^{43}	9.5×10^{40}	2.0×10^{43}
NGC 7212	9.1×10^{40}	8.2×10^{41}	1.2×10^{41}	5.2×10^{43}	1.3×10^{43}	4.2×10^{43}	5.4×10^{44}
Mrk 3	2.0×10^{41}	4.8×10^{43}	...	5.5×10^{43}	2.8×10^{44}

Note. — All luminosities are in units of erg s^{-1} .

^aObserved in nuclear spectrum, not corrected for absorption.

^bIntrinsic 2–10 keV luminosity, determined from Fe line luminosity.

^cLower limit on intrinsic 2–10 keV luminosity, determined from PEXRAV spectral model.

^dIntrinsic 2–10 keV luminosity, determined from $[\text{O III}]\lambda 5007$ luminosity.

^e8–1000 μm bandpass, from *IRAS* flux.

^fLower limit, from optical images.

Table 7. NGC 1068 Nucleus

E^a line	F^b line
$0.40^{+0.01}_{-0.03}$	350^{+180}_{-53}
0.55 ± 0.01	180^{+26}_{-14}
$0.71^{+0.10}_{-0.01}$	71^{+7}_{-8}
$0.87^{+0.14}_{-0.03}$	45^{+7}_{-6}
$0.99^{+0.03}_{-0.04}$	23^{+11}_{-6}
1.12 ± 0.02	16 ± 4
1.27 ± 0.30	10^{+3}_{-4}
$1.38^{+0.07}_{-0.14}$	6.8^{+3}_{-4}
$1.53^{+0.18}_{-0.10}$	4.7 ± 2
$1.66^{+0.09}_{-0.04}$	3.6 ± 2
1.88 ± 0.02	6.7 ± 2
$2.20^{+0.06}_{-0.4}$	3.3 ± 2
$2.51^{+0.09}_{-0.3}$	6.6^{+5}_{-2}
$3.23^{+5.7}_{-0.04}$	2.7^{+3}_{-4}
Additional Parameters	
χ^2/dof	45/42

Note. — Errors are 90% confidence limits for one interesting parameter.

^aEnergy of line center in keV.

^bLine flux in 10^{-5} photons $\text{cm}^{-2} \text{s}^{-1}$.

Table 8. Emission Measures

Galaxy (Region)	EM_{OVII} (cm^{-5})	EM_{NeIX} (cm^{-5})	$EM_{H\alpha}$ (cm^{-5})
ESO 428-G14 (center)	8.0×10^{20}	2.6×10^{21}	4.3×10^{24}
NGC 1386 (center)	1.2×10^{21}	1.7×10^{21}	2.1×10^{23}
NGC 3393 (center)	2.6×10^{21}	3.0×10^{21}	9.0×10^{22}
NGC 5347 (nucleus)	1.8×10^{21}	1.7×10^{21}	1.4×10^{24}

Table 9. Additional Sources

R.A.		Decl.		Count Rate	Distance	
(J2000)		(J2000)			(10^{-4} ct s $^{-1}$)	($''$)
<u>ESO 428-G14</u>						
7	16	25.22	-29 20	35.19	2.1 ± 1	102 12
7	16	25.45	-29 18	22.18	1.8 ± 1	100 11
7	16	26.41	-29 21	3.43	2.4 ± 1	113 13
7	16	26.75	-29 18	1.27	2.1 ± 1	105 12
7	16	27.30	-29 18	26.03	2.0 ± 1	81 9.1
7	16	27.66	-29 19	20.49	1.1 ± 1	47 5.3
7	16	29.23	-29 21	20.45	2.2 ± 2	114 13
7	16	29.95	-29 18	20.32	26 ± 3	70 8.0
7	16	30.07	-29 21	22.19	2.2 ± 1	114 13
7	16	30.29	-29 21	17.81	3.2 ± 2	110 12
7	16	30.63	-29 18	35.28	3.3 ± 2	54 6.1
7	16	30.80	-29 19	35.84	3.8 ± 2	9 1.0
7	16	31.50	-29 21	12.66	0.6 ± 1	104 12
7	16	31.85	-29 19	52.35	13 ± 3	25 2.8
7	16	31.93	-29 19	17.77	4.2 ± 2	15 1.7
7	16	32.37	-29 17	47.56	12 ± 2	103 12
7	16	33.01	-29 18	1.59	6.2 ± 2	91 10
7	16	34.02	-29 20	22.37	2.0 ± 2	65 7.4
7	16	37.06	-29 19	28.36	3.2 ± 2	77 8.7
7	16	37.31	-29 20	48.43	1.7 ± 1	113 13
7	16	37.33	-29 18	54.98	32 ± 4	87 9.9
7	16	37.63	-29 20	20.76	2.6 ± 1	99 11
<u>NGC 1386</u>						
3	36	37.36	-35 59	10.53	11 ± 2	117 7.0
3	36	39.17	-36 00	46.09	11 ± 2	98 5.9
3	36	39.56	-35 59	30.24	4.9 ± 2	85 5.1
3	36	39.58	-36 00	56.63	9.7 ± 2	100 6.0
3	36	43.56	-36 00	03.90	16 ± 3	32 1.9
3	36	44.18	-36 00	16.92	3.8 ± 2	31 1.9
3	36	46.31	-35 59	48.56	21 ± 3	9 0.5
3	36	46.50	-36 00	05.04	12 ± 3	9 0.5
3	36	46.75	-35 59	46.56	25 ± 4	13 0.8
3	36	47.32	-36 00	24.99	5.2 ± 2	31 1.9
3	36	47.61	-35 59	00.08	3.6 ± 1	60 3.6
3	36	50.22	-35 59	58.01	19 ± 3	49 2.9
3	36	51.77	-35 59	08.61	7.6 ± 2	84 5.0
<u>NGC 3393</u>						
10	48	15.67	-25 10	0.24	9.2 ± 2	107 28
10	48	17.66	-25 9	37.24	0.8 ± 1	79 20
10	48	19.13	-25 11	27.01	17 ± 3	119 31
10	48	26.01	-25 10	23.36	13 ± 3	53 14
10	48	26.03	-25 9	15.24	1.0 ± 1	45 12
10	48	27.64	-25 8	22.87	16 ± 3	99 26

Table 9—Continued

R.A. (J2000)			Decl. (J2000)			Count Rate (10^{-4} ct s $^{-1}$)	Distance ($''$) (kpc)	
10	48	30.61	-25	10	6.05	54 ± 5	100	26
<u>NGC 5347</u>								
13	53	8.33	33	29	35.45	2.4 ± 1	119	19
13	53	10.69	33	29	22.41	2.1 ± 1	89	14
13	53	17.72	33	29	8.25	2.3 ± 1	19	3.1
13	53	18.33	33	27	38.84	6.0 ± 2	109	18
13	53	23.85	33	30	31.41	6.2 ± 2	99	16
13	53	24.26	33	29	36.85	1.9 ± 1	81	13
13	53	24.39	33	28	38.76	2.3 ± 1	96	16
13	53	26.38	33	30	4.86	6.7 ± 2	114	18
<u>NGC 7212</u>								
22	06	54.36	10	14	09.02	9.1 ± 2	113	63
22	06	59.05	10	15	40.47	7.9 ± 2	108	60
22	06	59.68	10	13	13.03	9.3 ± 2	59	33
22	07	01.96	10	15	16.16	2.3 ± 1	75	42
22	07	02.54	10	14	16.08	7.9 ± 2	17	9.5
22	07	04.23	10	13	02.70	11 ± 2	67	37
22	07	04.85	10	14	22.53	3.8 ± 1	47	26
22	07	04.89	10	15	08.99	4.0 ± 1	80	44

Note. — Units of right ascension are hours, minutes, and seconds, and units of declination are degrees, arcminutes, and arcseconds.

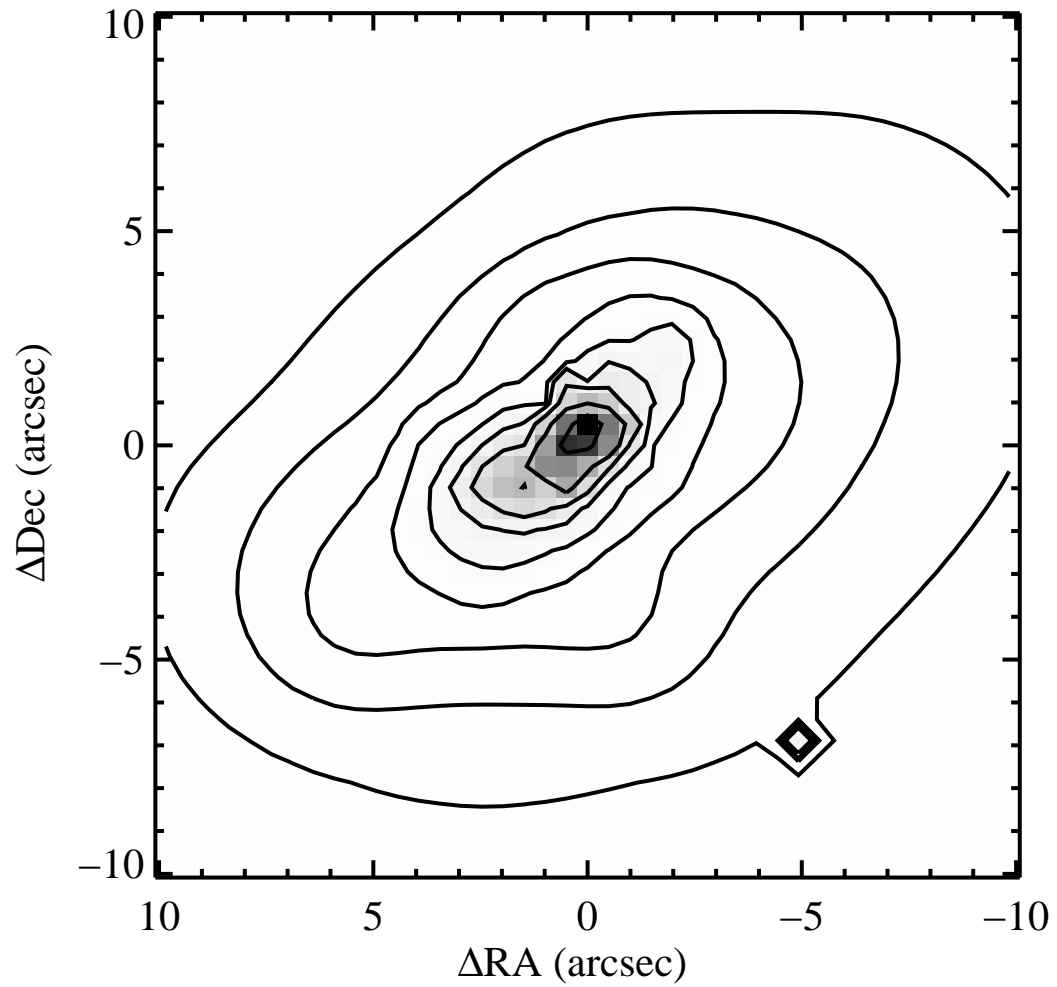


Fig. 1.— X-ray image of ESO 428-G14. The image has been adaptively smoothed and is scaled linearly. The contours are spaced logarithmically.

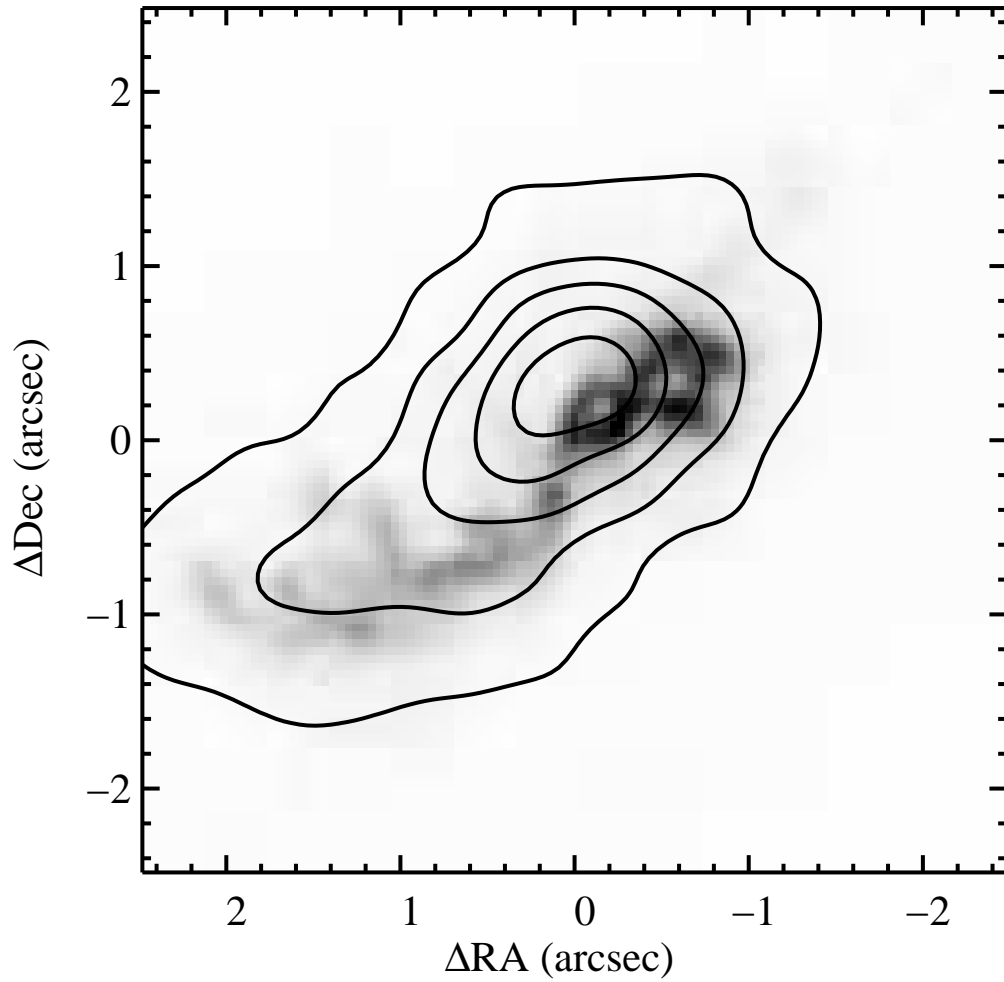


Fig. 2.— Continuum-subtracted H α image of ESO 428-G14 with linearly-scaled X-ray contours overlaid. The similar morphology of the X-ray and optical line emission suggests their common photoionized origin in all the sample members.

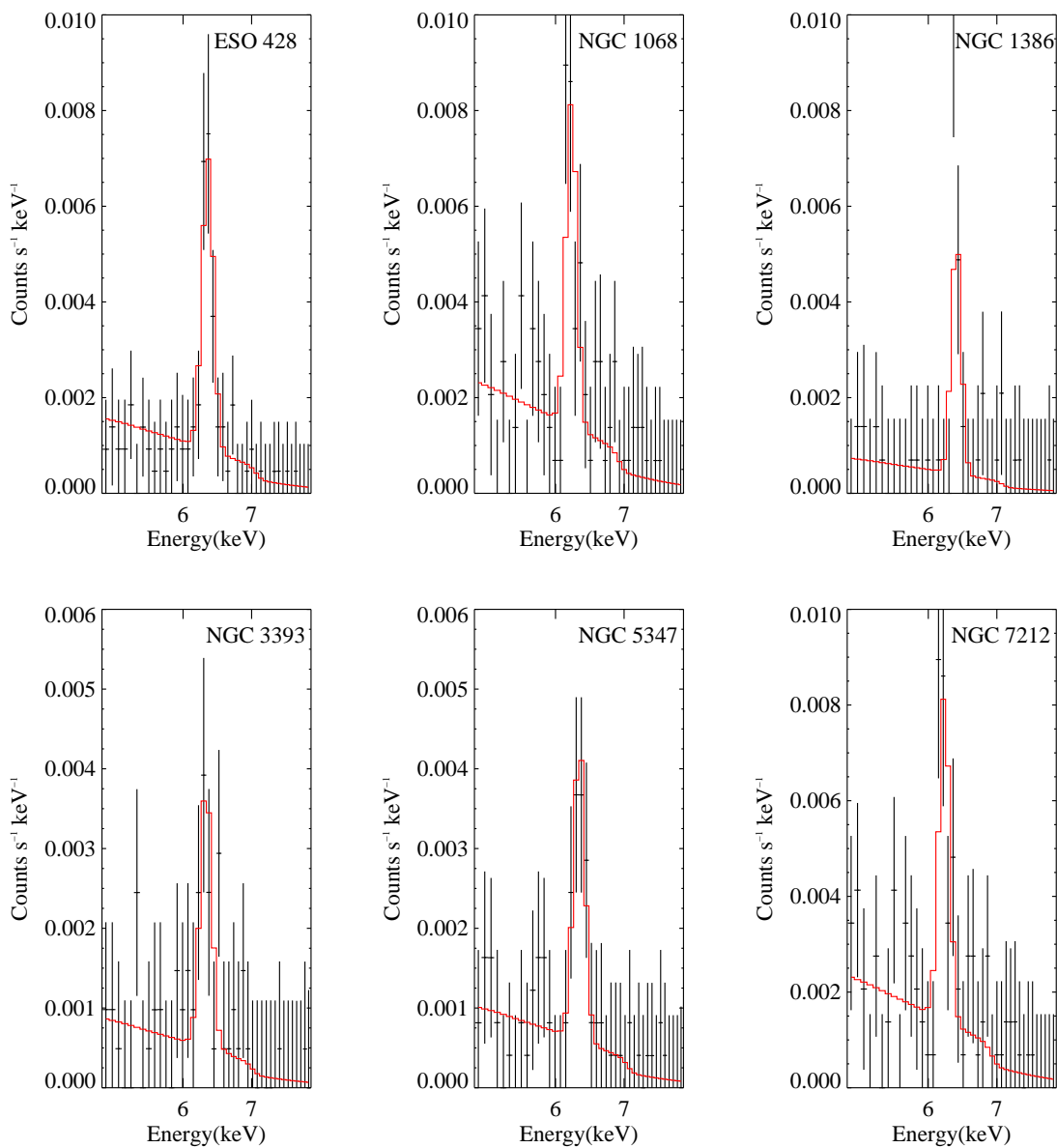


Fig. 3.— The prominent Fe $K\alpha$ lines are evident in all the observed nuclear spectra. The best-fitting model of the hard emission, which includes a pure reflection continuum and the emission line, is plotted with the data. We show binned data here but use the unbinned data in the model fitting.

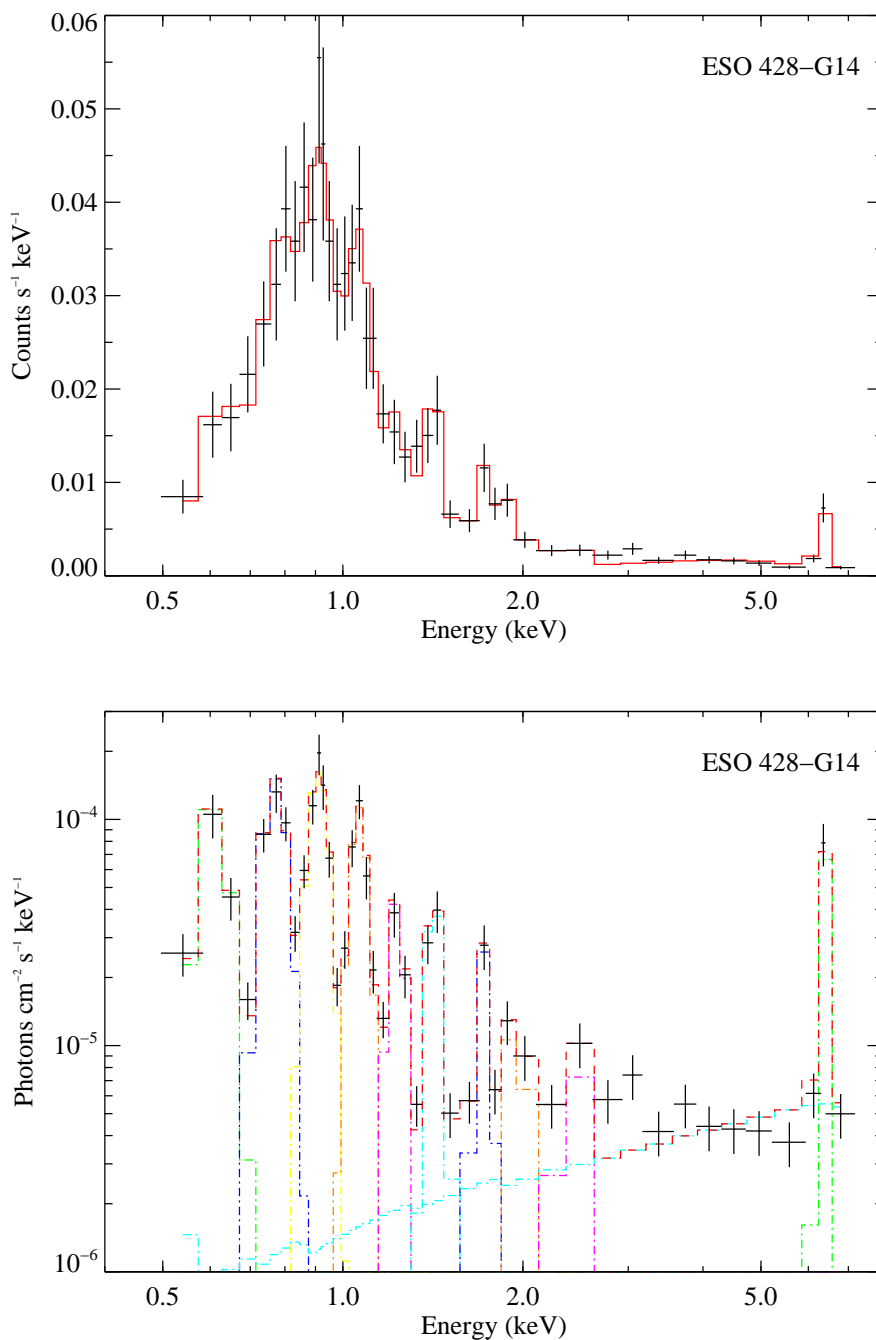


Fig. 4.— Nuclear spectrum of ESO 428-G14 (*crosses*) and best-fitting model (*red histogram*). (*upper panel*) Observed spectrum and total model, uncorrected for detector sensitivity. (*lower panel*) Emitted spectrum and model, corrected for detector sensitivity. Individual model components are plotted with dot-dashed lines. The hard X-ray spectrum shows the reflected AGN continuum and the Fe K α line, while 9 unresolved Gaussian line profiles account for the soft X-rays.

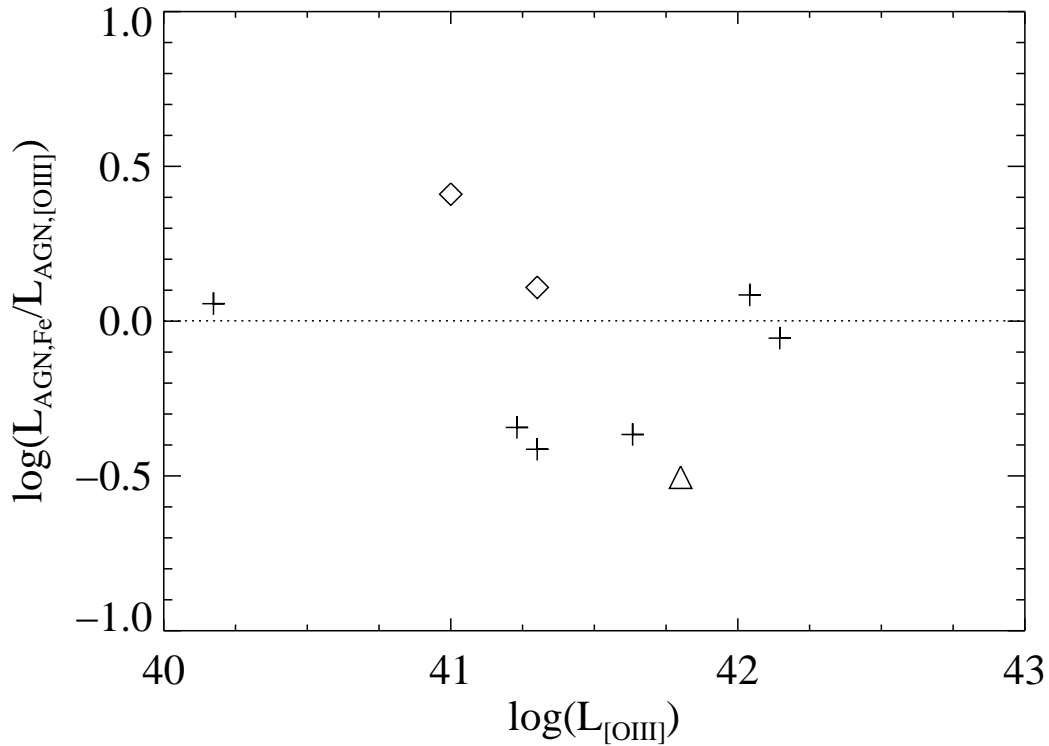


Fig. 5.— Ratio of intrinsic AGN 2–10 keV luminosity determined from the Fe $K\alpha$ line luminosity to intrinsic AGN 2–10 keV luminosity determined from the [O III] luminosity vs. [O III] luminosity. The luminosity is in units of erg s^{-1} . The sample members are plotted as crosses, except NGC 1068, which is plotted as a triangle. Two additional Compton thick galaxies from the literature that do contain circumnuclear starbursts (NGC 5135 and NGC 7130) are plotted as diamonds. The line is not a fit to the data and shows the good agreement of the two methods for determining intrinsic luminosity.

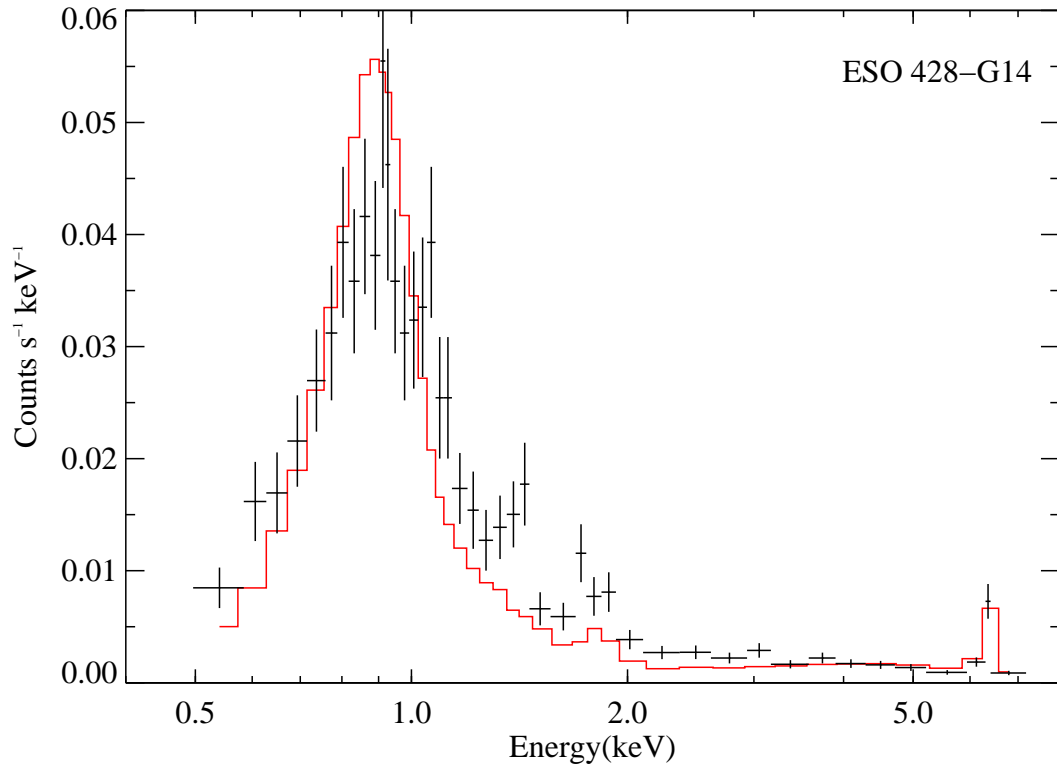


Fig. 6.— Nuclear spectrum of ESO 428-G14 fit with a thermal model ($kT = 0.7$ keV) in addition to the hard reflection components. The model fits the soft X-ray emission poorly, producing a broad emission hump around 0.9 keV, rather than the observed narrower features.

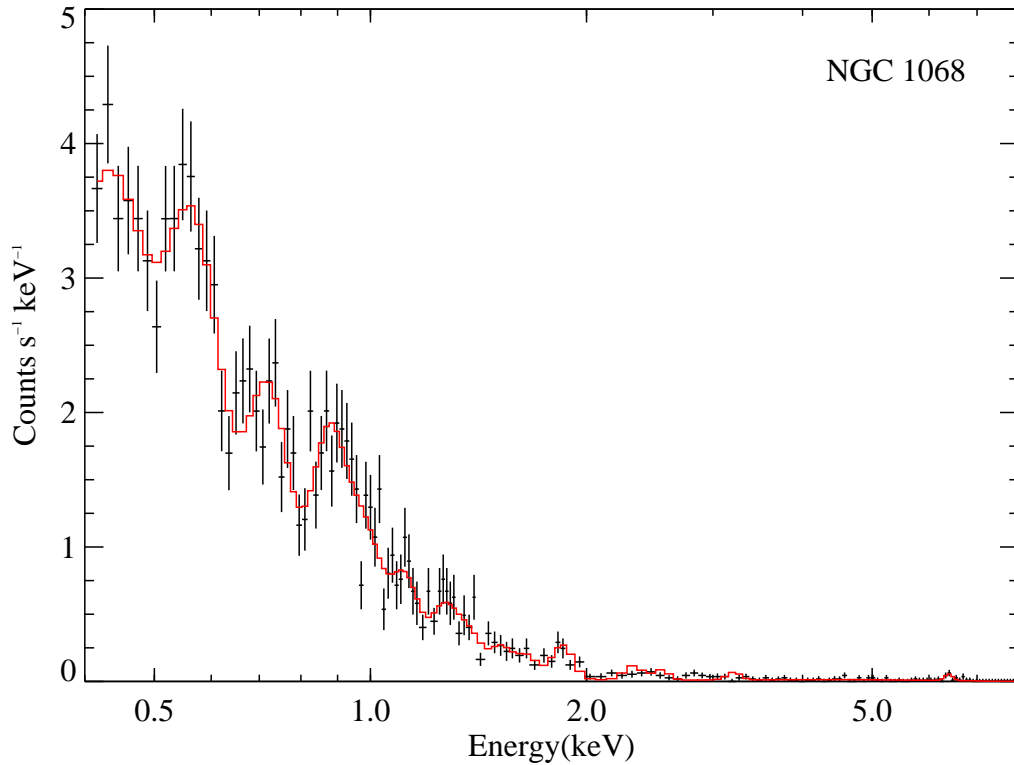


Fig. 7.— This ACIS spectrum of the nucleus of NGC 1068 shows narrow emission features, similar to the the ACIS spectra of the nuclei of the other galaxies. High spectral resolution observations of NGC 1068 confirm the dominant role of photoionization in producing the observed emission. The observed spectrum (*crosses*) and total model (*red histogram*), uncorrected for detector sensitivity, are plotted.

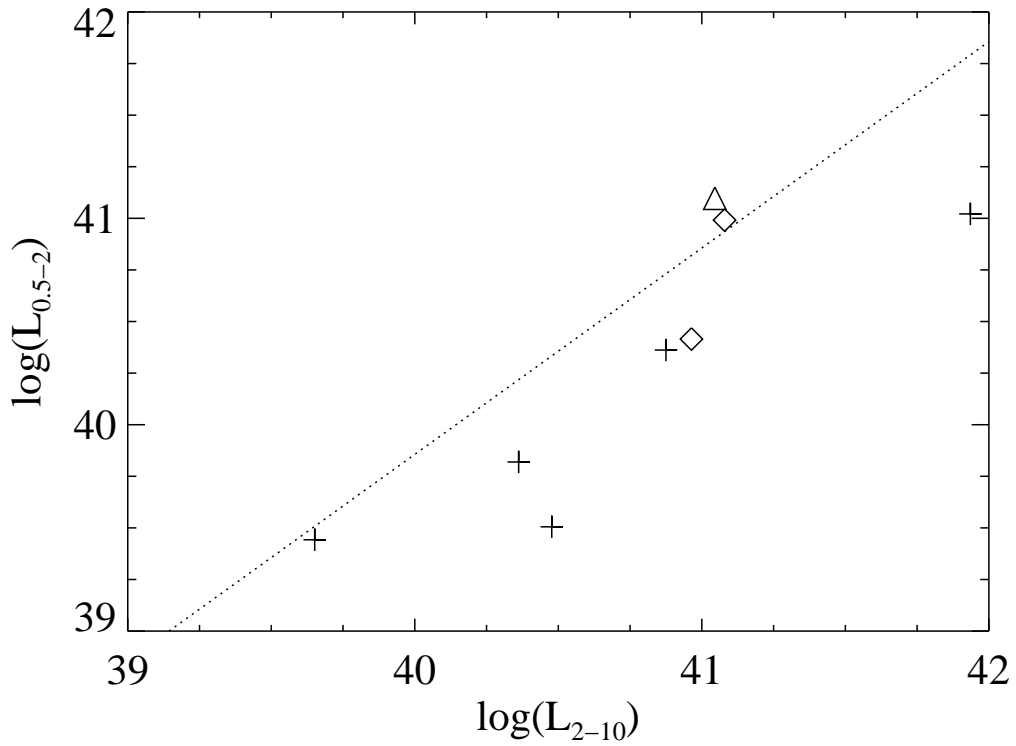


Fig. 8.— Observed soft (0.5–2 keV) vs. hard (2–10 keV) luminosity, uncorrected for absorption, in units of erg s^{-1} . The line is the relationship for a completely *unobscured* AGN, not a fit to the data. These Compton thick AGNs would appear to be unobscured and weak based on their hardness ratios alone. Symbols as in Figure 5.

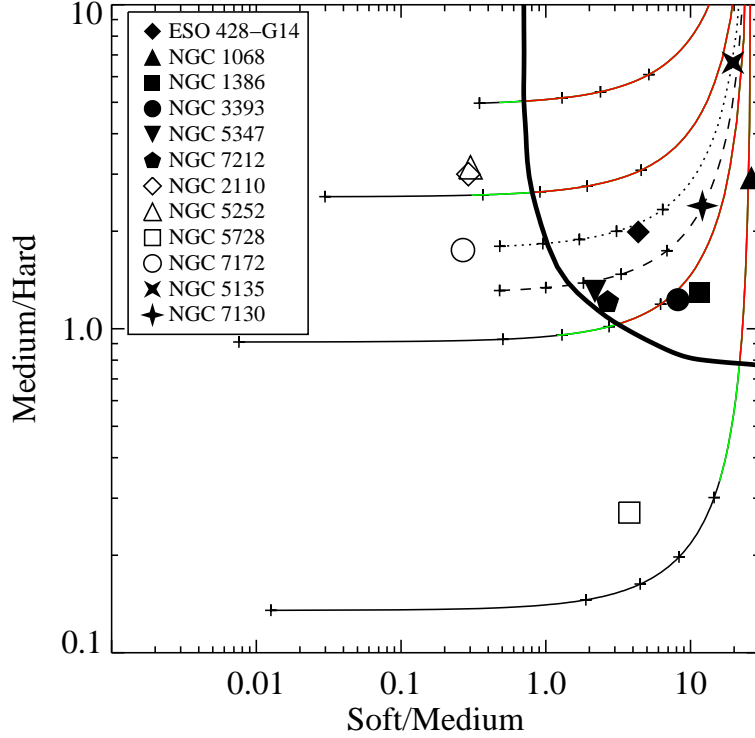


Fig. 9.— X-ray “color-color” plot, based on ratios of counts in the soft (0.3–2 keV), medium (2–5 keV) and hard (5–8 keV) bands that *Chandra* would observe. Each curve represents a different AGN continuum model. Solid curves show fixed AGN obscuration with $N_H = 3 \times 10^{22}$, 10^{23} , 3×10^{23} , and 10^{24} cm^{-2} (from top to bottom). Alternatively, the AGN contribution is calculated from the pure reflection model, either excluding (*dotted line*) or including (*dashed line*) an Fe K α line having EW = 1 keV. An empirical photoionization model is mixed with each of these AGN components. Along each curve, crosses are plotted where the photoionization model contributes 0, 20, 40, 60, and 80% of the total observed counts (from left to right). Thus, only the leftmost point of each curve describes a pure AGN model, one without any reflected or scattered soft X-ray component. A constraint on the efficiency with which the AGN continuum is converted into line emission excludes higher values of the soft/medium ratio in the moderate absorption models, distinguishing them from the reflection models. *Only Compton thick AGNs are found in the region to the right of the thick solid line.* Such colors would require excessively high reprocessing efficiency when absorption is Compton thin, with $L_{photo,0.5-2}/L_{AGN,2-10} \geq 0.03$. These strongly excluded regions of the moderately absorbed AGN models are also marked in red. Green identifies mixes where the reprocessing efficiency is high, with $0.01 < L_{photo,0.5-2}/L_{AGN,2-10} < 0.03$, although not strictly requiring Compton thick obscuration. The colors of galaxies of this study, the comparison Compton thick AGNs that also contain starbursts (both *filled symbols*), and several others that are not Compton thick (*open symbols*) are plotted.

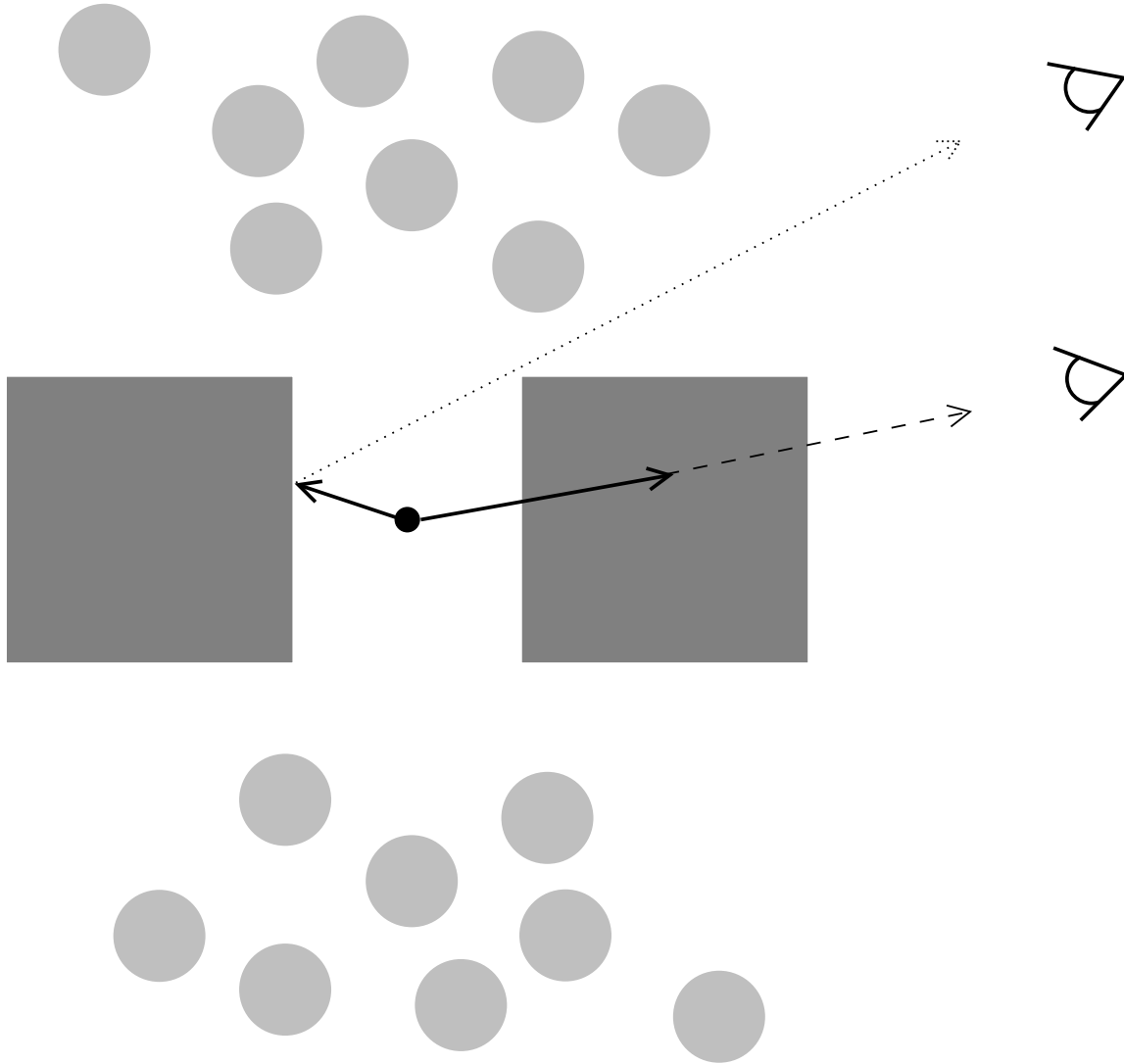


Fig. 10.— Two scenarios to observe the intrinsic AGN continuum (*solid lines*) in reflection, where an obscuring torus (*gray*) blocks direct views. For an observer at the right of the cartoon, the reflecting medium may be the far side of the torus, and the reflected light is not further obscured (*dotted line*). Alternatively, the blocking medium may also serve as the reflecting medium, in which case the reflected spectrum itself is obscured (*dashed line*). The unobscured continuum reaches the material of the photoionized emission region (*pale gray*). This figure is *not to scale*. The torus inner radius is on the order of 1 pc (the dust sublimation radius), while the photoionized emission extends over hundreds of pc.

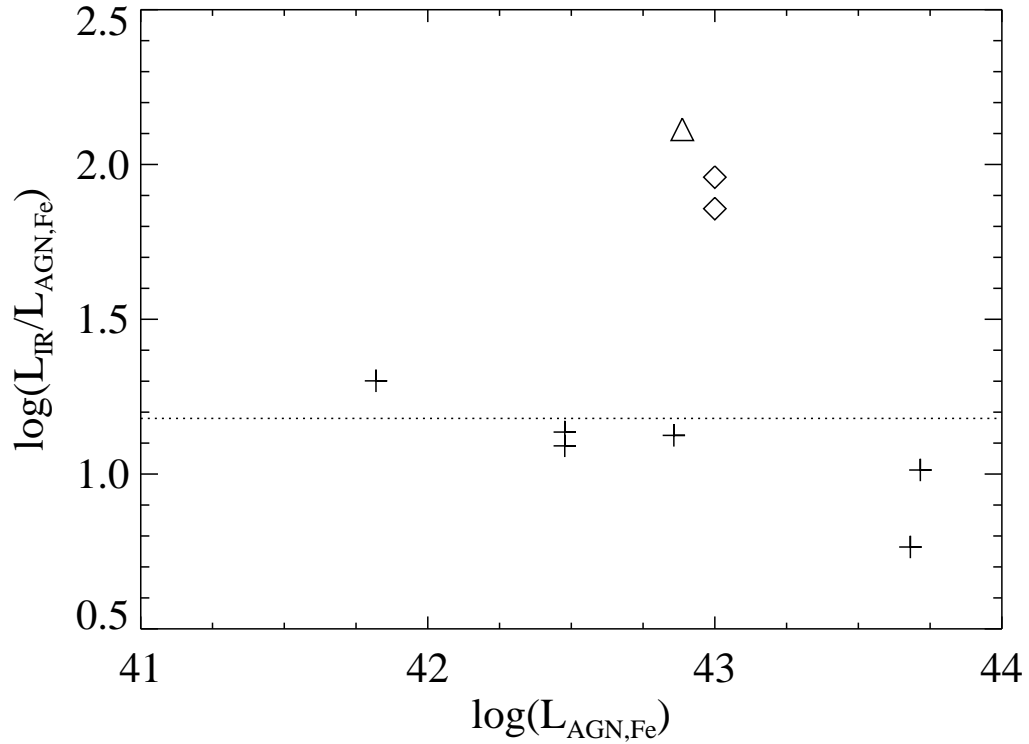


Fig. 11.— Ratio of total IR luminosity to intrinsic AGN 2–10 keV luminosity determined from the Fe $K\alpha$ line vs. intrinsic AGN luminosity determined from the Fe $K\alpha$ line. The luminosity is in units of erg s^{-1} . These Compton thick AGNs that do not contain starbursts (*crosses*) show IR/L_{AGN} ratios similar to unobscured AGNs (*dotted line*). The galaxies that do contain strong nuclear starbursts (*diamonds*) and NGC 1068 (*triangle*), which has a kpc-scale starburst, exhibit significant excess IR emission.

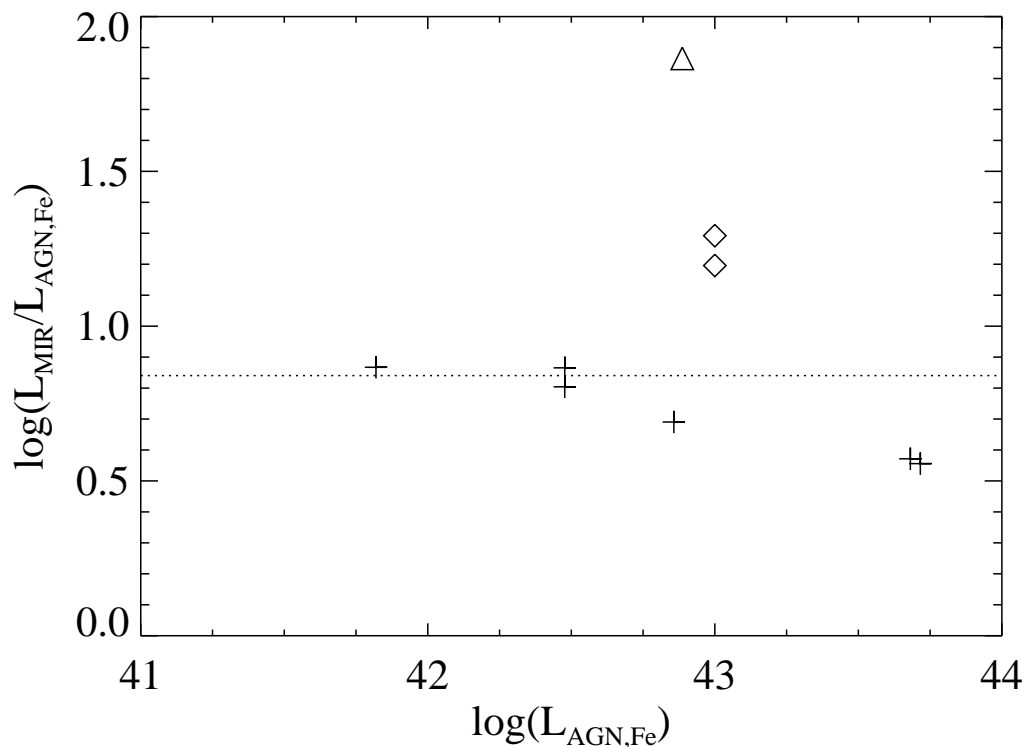


Fig. 12.— Ratio of mid-IR luminosity to intrinsic AGN 2–10 keV luminosity determined from the Fe $K\alpha$ line vs. intrinsic AGN luminosity determined from the Fe $K\alpha$ line. The luminosity is in units of erg s^{-1} . Similar to Figure 11, the luminosity ratios of the Compton thick AGNs that do not contain starbursts (*crosses*) are similar to those of unobscured AGNs (*dotted line*). While the mid-IR excesses of the starburst galaxies are less severe than their total IR excesses, mid-IR data alone do not accurately measure AGN luminosity when stellar contamination is significant.